Direct capsid labeling of infectious HIV-1 by genetic code expansion allows detection of largely complete nuclear capsids and suggests nuclear entry of HIV-1 complexes via common routes

Sandra Schifferdecker[1], Vojtech Zila[1], Thorsten G. Müller[1], Volkan Sakin[1], Maria Anders-Össwein[1], Vibor Laketa[1,2], Hans-Georg Kräusslich[1,2], Barbara Müller[1*]

[1] Department of Infectious Diseases, Virology, University Hospital Heidelberg, Heidelberg, Germany

[2] German Center for Infection Research, partner site Heidelberg, Germany

*To whom correspondence should be addressed: Barbara.mueller@med.uni-heidelberg.de

Keywords: HIV-1, capsid, click labeling, amber suppression, genetic code expansion, primary CD4$^+$ T cells, electron microscopy, correlative microscopy, STED, super-resolution microscopy

Abstract

The cone-shaped mature HIV-1 capsid is the main orchestrator of early viral replication. After cytosolic entry, it transports the viral replication complex along microtubules towards the nucleus. While it was initially believed that the reverse transcribed genome is released from the capsid in the cytosol, recent observations indicate that a high amount of capsid protein (CA) remains associated with subviral complexes during import through the nuclear pore complex (NPC). Observation of post-entry events *via* microscopic detection of HIV-1 CA is challenging, since epitope shielding limits immunodetection and the genetic fragility of CA hampers direct labeling approaches. Here, we present a minimally invasive strategy based on genetic code expansion and click chemistry that allows for site-directed fluorescent labeling of HIV-1 CA, while retaining virus morphology and infectivity. Thereby, we could directly visualize virions and subviral complexes using advanced microscopy, including nanoscopy and correlative imaging. Quantification of signal intensities of subviral complexes revealed an amount of CA associated with nuclear complexes in HeLa-derived cells and primary T cells consistent with a complete capsid and showed that treatment with the small molecule inhibitor PF74 did not result in capsid dissociation from nuclear complexes. Cone-shaped objects detected in the nucleus by electron tomography were clearly identified as capsid-derived structures by correlative microscopy. High-resolution imaging revealed dose-dependent clustering of nuclear capsids, suggesting that incoming particles may follow common entry routes.

43 **Introduction**

44 The cone-shaped capsid that encases the viral RNA genome and replication proteins
45 is a characteristic feature of infectious human immunodeficiency virus type 1 (HIV-1)
46 particles. Data obtained by many research groups over the past decade have revised
47 our understanding of the role of the mature capsid in HIV-1 replication, placing this
48 structure at the center stage of post-entry replication steps (reviewed in (Aiken and
49 Rousso, 2021; Engelman, 2021; James, 2019; Zila et al., 2021b). Upon fusion of the
50 virion envelope with the cell membrane, the capsid, which consists of ~1,200-1,500
51 monomers of the capsid protein CA (Briggs et al., 2003), is released into the cytosol.
52 It then usurps host cell factors to traffic towards the nucleus. Reverse transcription of
53 the viral RNA into dsDNA is initiated during passage of the subviral structure through
54 the cytosol. Following import into the nucleus, the viral dsDNA is covalently integrated
55 into the host cell genome by the viral integrase (IN). Prior to integration, the
56 surrounding capsid shell needs to release the dsDNA in a process termed uncoating.
57 The precise mechanisms, location, and timing of HIV-1 capsid uncoating are still under
58 investigation.

59 Initially, the HIV-1 capsid was presumed to rapidly dissociate upon cell entry, based
60 on little or no CA detected associated with isolated post-entry complexes (reviewed in
61 (Campbell and Hope, 2015)). Rapid or gradual disassembly in the cytosol was also
62 supported by several studies that applied fluorescence imaging to analyze subviral
63 complexes in infected cells (e.g., (Hulme et al., 2011; Mamede et al., 2017; Xu et al.,
64 2013). However, HIV-1 CA or the capsid lattice was found to directly engage in
65 interactions with various host factors involved in post-entry replication steps. Among
66 these capsid-interacting host factors are not only cytosolic proteins, including proteins
67 involved in microtubular transport, but also nucleoporins and even the nuclear protein
68 cleavage and polyadenylation specific factor 6 (CPSF6) (reviewed in (Engelman, 2021;
69 Naghavi, 2021; Saito and Yamashita, 2021)). These findings implied involvement of at
70 least a partial lattice structure in later stages of post-entry replication. Furthermore,
71 increasing evidence from imaging-based analyses argued for capsid uncoating at or
72 close to the nuclear pore (Burdick et al., 2017; Francis et al., 2020a; Francis et al.,
73 2016; Francis and Melikyan, 2018), or even indicated passage of (nearly) intact
74 capsids through nuclear pores (Burdick et al., 2020; Li et al., 2021; Muller et al., 2021;
75 Zila et al., 2021a). The recent detection of cone-shaped objects in the nuclear pore
76 channel and inside the nucleus by correlative light and electron microscopy (CLEM)

77 (Zila et al., 2021a), and intranuclear separation of CA or IN from reverse transcribed
78 dsDNA (Muller et al., 2021) also supported the model that the nucleus is the site of
79 HIV-1 uncoating (Muller et al., 2022).

80 One explanation for apparent discrepancies between different studies are the methods
81 that have been used for CA detection in fluorescence microscopy. Since the
82 modification of CA by genetic labeling strategies proved to be challenging, most studies
83 applied immunofluorescence (IF) staining or indirect labeling through a capsid binding
84 protein (e.g., (Burdick et al., 2017; Francis et al., 2016; Hulme et al., 2015; Mamede et
85 al., 2017; Peng et al., 2014; Zila et al., 2019)). A limitation of IF is that staining efficiency
86 may vary substantially depending on the antibody and detection conditions used, as
87 well as on differential exposure or shielding of epitopes due to conformational changes
88 or different intracellular environments. We could indeed show previously that
89 immunostaining efficiency of CA in the nucleus of host cells strongly depends on cell
90 type and experimental conditions (Muller et al., 2021). Furthermore, IF is incompatible
91 with live cell analyses. Infectious HIV-1 derivatives carrying fluorescent CA would
92 resolve these limitations and allow the direct observation of entering capsids with
93 quantitative analyses.

94 Direct genetic labeling of viral capsid proteins is challenging, however. Capsid proteins
95 are generally small proteins that need to assemble into ordered multimeric lattices. The
96 resulting assemblies must be stable during virus formation and transmission to a new
97 target cell, but also ready to disassemble in the newly infected cell, requiring structural
98 flexibility of the protomers. Beyond protein-protein interactions involved in capsid
99 assembly itself, capsid proteins generally undergo crucial interactions with other
100 components of the virion, e.g., the viral genome. Finally, the capsid surface represents
101 an essential contact interface between virus and host cell in the early phase of
102 infection, mediating cell entry in the case of non-enveloped viruses or interacting with
103 critical host cell dependency or restriction factors in the case of enveloped viruses.
104 Consequently, a large proportion of the surface exposed amino acids of a viral capsid
105 protein is involved in intermolecular contacts that are crucial for virus replication, which
106 renders these proteins highly susceptible to genetic modification. Fusion of a capsid
107 protein to a relatively large genetic label, e.g., green fluorescent protein (GFP) or other
108 fluorescent proteins, is thus generally prone to severely affect virus infectivity.

109 These considerations also apply to HIV-1 CA. The protein is encoded as a subdomain
110 of the structural polyprotein Gag, from which it is released by the viral protease (PR)
111 concomitant with virus budding to allow for formation of the mature capsid. With a
112 molecular mass of ~24 kDa, mature CA is of a similar size as GFP. CA hexamers are
113 the core structural elements of the immature Gag shell forming the nascent virus bud
114 in HIV-1 producing cells. Hexamers with a different conformation, together with 12 CA
115 pentamers that allow for bending and curvature, are the building blocks of the mature
116 capsid. CA pentamers, immature and mature hexamers employ different protein-
117 protein interfaces; together, these interfaces involve most of the exposed surface of
118 the CA monomer (reviewed in (Mattei et al., 2016)). Accordingly, scanning
119 mutagenesis analyses found HIV-1 CA to be highly genetically fragile (Rihn et al.,
120 2013; von Schwedler et al., 2003), with up to 89% of single amino acid exchanges
121 tested abolishing or severely affecting virus replication (Rihn et al., 2013). It is thus not
122 surprising that the introduction of genetically encoded labels - GFP or even a small
123 peptide tag - at various positions within HIV-1 CA have resulted in loss or severe
124 reduction of infectivity. Complementation with wild-type (wt) virus, from at least
125 equimolar amounts of wt CA to a substantial molar excess, was essential to restore
126 virus infectivity (Burdick et al., 2020; Campbell et al., 2008; Pereira et al., 2011; Zurnic
127 Bonisch et al., 2020). While the use of wt complemented particles can be sufficient for
128 fluorescent labeling, it is unclear whether the modified CA molecules are an integral
129 part of the mature CA lattice. Only approximately half of the CA molecules present
130 inside the virion are eventually used to form the mature capsid (Briggs et al., 2004;
131 Lanman et al., 2004), and CA fusion proteins may be preferentially excluded or less
132 stably integrated into the mature lattice.

133 We therefore established and applied a minimal invasive labeling strategy for HIV-1
134 CA based on genetic code expansion (GCE) and click labeling. This method involves
135 the exchange of a selected amino acid residue in the protein of interest with a non-
136 canonical amino acid (ncAA) carrying a highly reactive bio-orthogonal functional group
137 by a process termed amber suppression (Figure 1a). This residue is subsequently
138 covalently coupled to a fluorophore functionalized with a cognate reaction partner
139 (Figure 1a, b; reviewed in e.g. (Lang and Chin, 2014; Muller et al., 2019; Nikic and
140 Lemke, 2015)). Using this approach, we generated a CA-labeled HIV-1 derivative that
141 largely retained infectivity. In contrast to previous approaches for direct CA labeling,
142 our minimally modified derivative did not require complementation with wt virus. Direct

143 labeling with a bright and photostable chemical dye allows the application of various
144 imaging methods, i.e., live-cell imaging, super-resolution nanoscopy, or CLEM. The
145 click labeled virus variant thus enabled us to directly assess the amount of CA
146 associated with entering subviral complexes outside and within the nucleus of infected
147 HeLa-derived cells and primary $CD4^+$ T-cells, to visualize CA containing structures in
148 the nucleus by nanoscopy and correlative microscopy and to study the effect of the
149 CA-binding drug PF74 on the nuclear complexes.

150

151 **Results**

152 *Generation of an HIV-1 variant carrying a bio-orthogonal amino acid within CA*

153 To allow for minimally invasive labeling of HIV-1 CA by GCE (Figure 1), we introduced
154 an amber stop codon at a position of interest into the CA coding sequence within the
155 *gag* open reading frame of the proviral plasmid pNLC4-3 (Bohne and Krausslich,
156 2004). In order to avoid GCE modification of the accessory viral protein R (Vpr), which
157 is incorporated into the virion in high amounts (Muller et al., 2000), we first exchanged
158 the amber stop codon of *vpr* to an opal codon (TGA), resulting in plasmid pNLC4-3*.
159 Although this mutation did not alter the coding sequence of viral proteins or virion
160 infectivity (Figure S1), the corresponding virus was termed HIV-1* to indicate the
161 modification. Since neither the efficiency of amber suppression in a given sequence
162 context in eukaryotic cells, nor the effect of ncAA incorporation on viral functionality
163 can be predicted with certainty, we tested a panel of 18 amber mutations at sites
164 located towards the outer surface of the capsid lattice for suppression efficiency and
165 virus infectivity (Schifferdecker, Sakin et al., in preparation). Based on a comparison of
166 Gag expression levels and viral infectivity upon ncAA incorporation, we selected a virus
167 variant in which residue alanine 14 in CA was replaced by a non-canonical amino acid
168 (HIV-1*CA14^{ncAA}) for further analyses.

169 For virus preparation, HEK293T cells were co-transfected with the respective mutant
170 proviral plasmid and pNESPylRS-eRF1dn-tRNA. The latter plasmid encodes for a
171 complete amber suppression system, consisting of modified tRNA, a cognate
172 genetically engineered pyrrolysine aminoacyl-tRNA synthetase (Nikic et al., 2016), and
173 a dominant-negative version of the eukaryotic release factor eRF1 that improves
174 amber suppression efficiency in eukaryotic cells (Schmied et al., 2014). To produce
175 functionalized virus particles, cells were grown in the presence of the small ncAA

176 cyclopropene lysine (CpK). While truncation of Gag at position 14 of CA would prevent
177 virus formation, incorporation of CpK by amber suppression should result in the
178 expression of full-length Gag and thereby promote HIV-1 particle assembly.
179 Immunoblot analysis of cell lysates indeed demonstrated the presence of full-length
180 Gag polyprotein precursor when HIV-1*CA14^{TAG} expressing cells were grown in the
181 presence of CpK, whereas full-length Gag was not detected when CpK was omitted
182 from the growth medium (Figure S2a). Thin-section electron microscopy (EM) revealed
183 late budding sites and immature- as well as mature-like virions at the plasma
184 membrane and in the vicinity of HIV-1*CA14^{TAG} expressing cells, that were
185 morphologically indistinguishable from typical HIV-1 wild-type (wt) budding sites and
186 virions (Figure 2a). Virus release efficiency from transfected cells, as estimated by
187 immunoblot analysis of cell and particle lysates, was comparable for wt and HIV-
188 1*CA14^{CpK} (Figure S2b). We concluded that Gag expression of HIV-1*CA14^{TAG} is
189 ncAA dependent and the modified CA domain is competent for immature and mature
190 lattice assembly.

191

192 *Characterization of click labeled HIV-1 virions*

193 We next prepared virus particles from the supernatant of HIV-1*CA14^{ncAA} producing
194 cells and subjected them to click labeling using the membrane-permeable dye silicon
195 rhodamine tetrazine (SiR-Tet; (Lukinavicius et al., 2013); Figure 1b), generating HIV-
196 1*CA14^{SiR}. As a control, HIV-1* wt particles were prepared under amber suppression
197 conditions and stained in parallel. Consistent with the detection of viral assembly sites
198 and particles in electron micrographs of transfected cells (Figure 2a), virus was
199 recovered from the tissue culture supernatant of HIV-1*CA14^{ncAA} expressing cells.
200 Particle yields were moderately reduced compared to the HIV-1* wt control, in line with
201 the fact that amber suppression is usually incomplete in eukaryotic cells (optimal ncAA
202 incorporation efficiencies in the range of ~25-50 %; e.g., (Sakin et al., 2017; Schmied
203 et al., 2014). On average, we obtained 5-10-fold lower yields for HIV-1*CA14^{SiR}
204 compared to HIV-1* as determined by RT activity (Figure 2b) and CA content (Figure
205 2c) of particle preparations. Comparison of stained and unstained preparations
206 demonstrated that particle yield, assessed by RT activity of virus preparations, was not
207 affected by the click-labeling procedure (Figure S3). Consistent with the observation of
208 morphologically mature particles by EM, click labeled particles displayed regular Gag

209 and GagPol processing products (Figure 2d), with clear bands for mature CA (p24)
210 and mature RT heterodimer (p51, p66).

211

212 *Fluorescence labeling and infectivity of click labeled virions*

213 In order to determine fluorescence staining specificity, particle lysates of HIV-1* and
214 HIV-1*CA14^{CpK} stained with Tet-SiR were analyzed by SDS-PAGE followed by in-gel
215 fluorescence measurement (Figure 3a). The resulting image revealed a distinct SiR
216 labeled band corresponding to a mass of approximately 24 kDa and weak bands
217 corresponding in size to CA containing precursors in the case of HIV-1*CA14^{SiR},
218 whereas fluorescent protein bands were undetectable for the HIV-1* control (Figure
219 3a, bottom panel). Subsequent immunoblotting of the scanned gel using antiserum
220 raised against CA ensured that similar amounts of virus particles had been loaded for
221 wt and the CA14 variant (Figure 3a, top panel). These results indicated specific GCE-
222 dependent labeling of CA *via* amber suppression at position 14 of HIV-1 CA.

223 To test efficiency of SiR staining, labeled particles adhered to a glass chamber slide
224 were fixed, permeabilized, immunostained with antiserum raised against HIV-1 CA to
225 validate that detected signals corresponded to virus particles and imaged by confocal
226 microscopy (Figure 3b, c). Confocal micrographs were recorded in the channels
227 corresponding to the CA (IF) stain (green) and direct CA labeling with SiR (magenta).
228 Regions of interest (ROIs) corresponding to the position of virus particles were defined
229 based on CA(IF) signals. Measurement of SiR fluorescence intensities in these ROIs
230 revealed only weak background staining in the case of HIV-1* (Figure 3b). In contrast,
231 distinct SiR signals co-localizing with CA(IF) punctae were detected for HIV-1*CA14^{SiR}
232 (Figure 3c). Quantitative analyses of images from multiple independent experiments
233 confirmed this visual impression (Figure 3d, e). Only ~8.5% of HIV-1* particles were
234 classified as SiR positive, with fluorescence intensities only slightly above the
235 background level (~1,000 a.u.; Figure 3d). In contrast, >95% HIV-1*CA14^{SiR} particles
236 displayed clear SiR staining, with a mean fluorescence intensity of ~15,000 a.u. (Figure
237 3e). Variation in SiR fluorescence intensities between individual particles is expected,
238 since particle size and CA content of HIV-1 virions varies, with ~1,700-3,100 CA
239 monomers estimated per particle (Carlson et al., 2008). Beyond that, the range of SiR
240 signal intensities observed also indicated a range of click labeling efficiencies. Despite
241 variable staining intensities within the preparation, the vast majority of HIV-1*CA14^{CpK}

242 particles could be efficiently click labeled with SiR, attaining fluorescence intensities
243 suitable for fluorescence microscopy of infected cells.

244 To test the effect of introducing a synthetic fluorophore at position 14 on CA
245 functionality, the infectivity of click labeled particles was assessed by titration of labeled
246 particles on TZM-bl cells, followed by immunostaining against the HIV-1 matrix protein
247 (MA) to identify infected cells. As shown in Figures 3f and g, relative infectivity of HIV-
248 1*CA14^{SiR} was only mildly reduced by an average of ~2-fold compared to HIV-1*. This
249 moderate reduction in infectivity represented a substantial improvement compared to
250 previous genetically labeled derivatives in the absence of complementation (Burdick et
251 al., 2020; Campbell et al., 2008; Pereira et al., 2011; Zurnic Bonisch et al., 2020). Thus,
252 minimal invasive labeling by GCE allows direct labeling of HIV-1 CA without requiring
253 complementation with wt virus.

254

255 *Detection of click labeled HIV-1 in infected cells*

256 Having established a suitable labeling strategy, we used labeled particles to infect and
257 image target cells. Initial experiments were performed in the model cell line HeLa TZM-
258 bl. Cells infected with HIV-1*CA14^{SiR} at a multiplicity of infection (MOI) of ~0.8 were
259 fixed at 18 h post infection (p.i.). Immunostaining with antiserum against CA was
260 performed under conditions that allow for immunodetection of cytosolic and nuclear
261 complexes (Muller et al., 2021) to test whether detected SiR signals corresponded to
262 HIV-1 particles. Labeled particles could be visualized by spinning disc confocal
263 microscopy (SDCM) in the cellular environment (Figure 4a, Figure S4 and S5).
264 Confocal images revealed punctate SiR signals in the cytosol, close to the nuclear
265 envelope and within the nucleus of infected cells. Co-localization with CA(IF) staining
266 confirmed that these signals represented entering viral structures (Figure 4a, Figure
267 S4 and S5).

268 Next, TZM-bl cells infected with HIV-1* or HIV-1*CA14^{SiR} were fixed and analyzed for
269 the presence of click labeled subviral particles inside the nucleus at different time
270 points after infection. Consistent with earlier results (Zurnic 2020, Burdick 2020, Müller
271 2021), we observed nuclear CA(IF) positive foci in HIV-1* infected cells as early as 6
272 h p.i. (Figure 4b, black), while such signals were absent in noninfected cells (Figure
273 4b, grey). Importantly, we detected SiR positive complexes in the nucleus of HIV-
274 1*CA14^{SiR} infected cells, with the vast majority also positive for CA(IF) (Figure 4b, red).

275 Nuclear entry appeared to be delayed for HIV-1*CA14^{SiR} compared to HIV-1* by 6-12
276 h. Nevertheless, samples infected with HIV-1*CA14^{SiR} displayed a comparable
277 proportion of cells with detectable capsid-like objects in the nucleus as the HIV-1*
278 infected control at 12 h p.i. (Figure 4b). The same was true for the number of nuclear
279 objects detected per cell (Figure 4c); at 12 h p.i., HIV-1*CA14^{SiR} reached an average
280 of 4.58 $\pm$ 4.12 nuclear particles per cell, similar to HIV-1* with 5.91 $\pm$ 4.11.

281 Delayed detection of subviral complexes in the nucleus may be due to slower uptake,
282 slower trafficking towards the nuclear envelope, delayed passage through the NPC, or
283 a combination thereof. In order to distinguish between these possibilities, we extended
284 the time-resolved quantification to objects in close vicinity to the nuclear envelope
285 (Figure 4d). This analysis revealed that the HIV-1*CA14^{SiR} derived subviral structures
286 reached the nuclear envelope with similar kinetics as HIV-1* particles (Figure 4d, NE
287 assoc.). A comparable average proportion of CA containing objects was detected at
288 the nuclear envelope in both cases at 6 h p.i., while the numbers of nuclear capsids
289 were lower for HIV-1*CA14^{SiR} at that time (Figure 4d, Nucleus). In contrast, the highest
290 proportion of HIV-1*CA14^{SiR} nuclear objects with 4.20 $\pm$ 1.80% was detected at 18 h
291 p.i., while HIV-1* reached similar levels at 6 h p.i. This implies that the mechanistic
292 action of the capsid in nuclear import underlies tight margins with respect to its
293 biophysical properties.

294

295 *Characterization of nuclear CA^{SiR} containing complexes*

296 A long-standing question in the field of HIV-1 early replication is when and where
297 genome uncoating takes place. The possibility to directly detect CA molecules clicked
298 to a synthetic fluorophore enabled us to assess the amounts of CA associated with
299 subviral complexes at different intracellular sites, without the influence of differential
300 epitope accessibility or of a tag domain that potentially confers different properties to a
301 subpopulation of CA molecules. However, comparing labeling intensities for nuclear,
302 cytoplasmic, and extracellular particle-associated structures may be additionally
303 confounded in diffraction-limited microscopy by the failure to resolve closely adjacent
304 individual capsids. Clusters of nuclear capsids had indeed been observed by CLEM
305 analyses in our previous study (Muller et al., 2021).

306 To determine whether nuclear cluster formation occurred under our conditions, we
307 exploited the fact that the chemical dye conjugated to the capsid surface renders the

308 modified virus suitable for super-resolution microscopy. With a lateral resolution of <50
309 nm, STED nanoscopy allows visual separation of closely adjacent CA objects. TZM-bl
310 cells were infected with HIV-1*CA14^{SiR} at two different MOIs. MOI~0.8 corresponded
311 to the conditions generally used in our experiments; a 10-fold higher virus dose (MOI
312 ~8) was applied in a parallel experiment to test for enhancement of capsid clustering.
313 At 18 h p.i., cells were fixed, immunostained against CA, and imaged using a STED
314 system in confocal and STED mode (Figure 5). Nuclear CA(IF)/(SiR) double-positive
315 objects were detected under both conditions (Figure 5a, arrowheads). While these
316 objects appeared as individual punctae in diffraction-limited micrographs from the IF
317 and SiR channels at both MOIs (Figure 5b, top and middle row), imaging of the SiR
318 channel in STED mode revealed differences between individual punctae. Some
319 diffraction-limited punctae in the nucleus represented individual capsid-like objects
320 when imaged by STED (Figure 5b, left panel, bottom row). In contrast, other punctae
321 were resolved into small clusters of 2-4 closely apposed CA-containing objects by
322 super-resolution microscopy (Figure 5b, right panel, bottom row), consistent with
323 observations made by electron tomography (Muller et al., 2021; Zila et al., 2021a). A
324 quantitative analysis of cluster sizes (Figure 5c) revealed that the propensity for capsid
325 clustering in the nucleus correlated with the amount of virus used for infection.
326 Consistent with a normal distribution of infection events per cell at a given MOI, ~50%
327 of those cells positive for nuclear punctae displayed only a single STED resolved object
328 at MOI 0.8, whereas all cells analyzed at MOI 8 comprised more than one STED
329 resolved nuclear object, with up to 15 objects identified in one nucleus (Figure S6).
330 Accordingly, at MOI~0.8, the vast majority of punctae (~88%) corresponded to
331 individual capsid-like objects in the nucleus, and clusters of more than two objects were
332 not observed. In contrast, the majority of cells analyzed comprising more than one
333 nuclear object displayed clustered particles, and almost half of the nuclear punctae
334 (~43%) corresponded to clusters of 2-4 objects when cells were infected with MOI~8.
335 We conclude that nuclear capsid clustering is rarely observed at the MOI of 0.8 used
336 throughout this study, and that nuclear clustering appears not to be a random event.
337 The previously observed capsid clustering in distinct nuclear positions as well as larger
338 clusters occurred preferentially at high MOI, where a higher proportion of cells
339 contained multiple nuclear particles.

340 We next proceeded to SiR fluorescence intensity measurements, comparing the signal
341 intensity of extranuclear HIV-1 particles to that of subviral structures in the nucleus.

342 Staining of the plasma membrane with mCLING ATTO488 before infection revealed
343 that under our conditions most cell-associated particles in the cytosolic region
344 represented virions present in endosomes, corresponding to a pre-fusion state of the
345 virus (Figure S7a-c). To ensure that these extranuclear punctae represented single
346 objects, cytoplasmic foci were analyzed in STED mode. We found that ~95% (n=79)
347 of analyzed punctae corresponded to an individual object, while only ~5% (n=4) of
348 these foci were resolved into two adjacent objects by nanoscopy (Figure S8).

349 As illustrated by the cartoon in Figure 6a, complete virions comprise on average ~2,400
350 CA molecules, while only ~1,200-1,500 of these are part of the mature fullerene capsid
351 (Briggs 2003, Carlson 2008, Lanman 2004) that represents a post-fusion state.
352 Assuming equal click labeling efficiency of $CA14^{CpK}$ for molecules that are part of the
353 mature lattice and those that remain free in the virion volume, the average SiR intensity
354 of complete capsids is expected to correspond to ~50-60% of the average intensity of
355 complete virions from the same preparation. We infected TZM-bl cells at an MOI of 0.8
356 and quantified the SiR intensity of virions attached to the cell or in the cytosolic region
357 (and thus mostly in endosomes) as well as nuclear punctae (Figure 6b). As a control,
358 we compared SiR intensities of the small proportion of mCLING-negative (post-fusion)
359 structures in the cytoplasmic region with that of mCLING positive (endosomal) objects.
360 This analysis revealed an average SiR intensity of ~ 66% for mCLING negative
361 compared to mCLING positive objects (Figure S7d), indicating that we can reliably
362 differentiate between complete virions and post-fusion complexes based on intensity
363 of CA staining. The average SiR intensity of >6,000 cell-attached and (mostly)
364 endosomal particles in the cytosolic region exhibited an average of 17,649 a.u.. In
365 contrast, the SiR intensity of >100 nuclear subviral structures averaged 9,835 a.u.
366 (Figure 6b), i.e., ~ 56% of the average intensity of complete virions, similar to the
367 predicted relative CA content of the mature capsid and similar to the intensity of
368 mCLING-negative cytoplasmic objects. Based on these findings, we conclude that the
369 CA(SiR) containing objects in the nuclei of these cells correspond approximately to the
370 full CA complement of the mature capsid.

371 The small molecule inhibitor PF74 (Blair et al. 2010) binds to the HIV-1 capsid in a
372 pocket overlapping the binding sites for the FG motifs of various nucleoporins and for
373 the nuclear host protein CPSF6 (Bhattacharya et al., 2014; Matreyek et al., 2013; Price
374 et al., 2012). This compound inhibits HIV-1 replication by multiple mechanisms, with
375 effects on different replications steps reported based on PF74 concentration and time

376 of addition (reviewed in (Thenin-Houssier and Valente, 2016)). Treatment with high
377 concentrations of PF74 has been reported to destabilize the capsid (Burdick et al.,
378 2020; Shi et al., 2011), but data obtained in recent studies argued against a PF74
379 induced loss of CA from nuclear complexes (Muller et al., 2021) and even showed an
380 increased CA(IF) signal (Francis et al., 2020b). These findings are consistent with a
381 stabilizing effect of the compound on the capsid lattice observed for isolated capsids
382 after initial opening (Marquez et al., 2018; Rankovic et al., 2018), and for *in vitro*
383 assembled CA-NC particles (Dostalkova et al., 2020). Since results obtained by
384 immunodetection may be influenced by differential CA epitope exposure, we revisited
385 this issue employing direct CA labeling. TZM-bl cells were infected with HIV-1*CA14^{SiR}
386 particles for 17 h and then treated with 2-15 µM PF74 or DMSO for 1 h, followed by
387 fixation, permeabilization, methanol extraction, and SDCM imaging. CA(SiR) punctae
388 detected in the nucleus of DMSO control cells were positive for CPSF6 (Figure 6c ii).
389 Intensity profile measurement revealed clear colocalization of both signals indicating
390 that direct capsid labeling did not affect association with CPSF6 (Figure 6d). In
391 accordance with earlier results (Francis et al., 2020b; Muller et al., 2021), CA(SiR)
392 positive subviral complexes in nuclei of cells subjected to PF74 treatment lacked
393 CPSF6 association (Figure 6e, and 6f). Their mean CA(SiR) intensity remained
394 unaltered, however, indicating that the capsid remains largely stable in the presence
395 of PF74 concentrations ranging from 2-15 µM (Figure 6g).

396

397 *Detection of directly labeled HIV-1 capsids in primary cells*

398 To validate our results in a physiologically relevant cell type, primary human CD4^{+} T
399 cells from healthy blood donors were infected, subjected to IF staining against CA, and
400 imaged by SDCM at 24 h p.i. (Figure 7a and Figure S9). We readily detected nuclear
401 subviral SiR positive structures in HIV-1*CA14^{SiR} infected cells, indicating that nuclear
402 replication complexes retained CA also in these primary cells (Figure 7a). Consistent
403 with prior observations made in T cell lines (Zila et al., 2019) the majority of SiR-positive
404 objects were not associated with CA(IF) signals (9/11 particles; Figure 7a, left and
405 Figure S9a) when fixation and immunostaining were performed under standard
406 conditions. As outlined above, treatment with 15 µM PF74 for 1 h dissociates the large
407 clusters of CPSF6 from nuclear subviral complexes. We observed that this in turn
408 renders nuclear CA accessible for IF detection in T cells, presumably by exposure of

409 CA epitopes upon CPSF6 displacement (Muller et al., 2021). Accordingly, brief PF74
410 treatment allowed for detection of CA(IF) signals co-localizing with nuclear CA(SiR)
411 punctae (13/16; Figure 7a, right and Figure S9b). We conclude that the direct CA
412 labeling strategy presented here overcomes technical artifacts that hamper IF
413 analyses.

414 Further quantitative analyses using primary $CD4^+$ T cells prepared from six blood
415 donors revealed similar numbers of nuclear capsid structures in cells infected with HIV-
416 1*$CA14^{SiR}$ compared to cells infected with HIV-1* at 24 h p.i. (Figure 7b). SiR intensity
417 measurements were only performed for intranuclear objects in this case, since high
418 background due to SiR accumulation in the narrow cytoplasm of T cells precluded
419 reliable analysis of individual particles in the extranuclear region. Quantitation of SiR
420 intensities of nuclear punctae in cells infected with a MOI~0.8 yielded similar average
421 intensities as measured in TZM-bl cells (mean=12,485 a.u.), indicating the presence
422 of a complete or nearly complete mature capsid in the nuclear complexes in primary T
423 cells as well (Figure 7c). Cells infected with a MOI of ~8 displayed higher CA(SiR)
424 intensities of diffraction-limited nuclear objects (mean=39,502 a.u.), suggesting
425 intranuclear clustering of capsids, as observed in TZM-bl cells (Figure 5).

426 Our findings from CA(SiR) intensity measurements argued for the presence of a full
427 capsid complement at subviral structures in the nucleus. These data strengthen
428 conclusions from several recent studies suggesting that the mature capsid lattice may
429 be completely or largely intact on nuclear subviral objects (Burdick et al., 2020; Muller
430 et al., 2021; Zila et al., 2021a). However, fluorescence signals do not yield information
431 on the architecture of nuclear $CA14^{SiR}$ containing objects. Therefore, we
432 complemented our analyses by performing CLEM of infected SupT1 T cells. In order
433 to maximize the number of nuclear objects, infection was synchronized by the
434 attachment of particles to the cells for 3 h at a low temperature (16°C) to prevent
435 particle uptake by membrane fusion or endocytosis (Melikyan et al., 2000; Weigel and
436 Oka, 1981). Virus entry was initiated by temperature shift to 37°C. At 24 h post
437 temperature shift, specimens were prepared by high-pressure freezing and freeze
438 substitution. 250 nm thick resin sections were subjected to SDCM in order to localize
439 CA(SiR) containing structures, followed by correlative electron tomography (CLEM-
440 ET) analysis. CA(SiR) positive objects could be identified by SDCM in the sections
441 (Figure 7d), demonstrating that the brightness of signals derived from direct CA(SiR)
442 labeling is sufficient for CLEM detection of cytosolic and nuclear (sub)viral structures.

443 ROIs were defined based on the SiR signals and subjected to correlative ET analysis.
444 Figure 7e shows an exemplary tomogram obtained from a ROI located within the
445 nucleus. It reveals several closely apposed electron-dense structures at the position of
446 the SiR label, whose shape and dimension match those of intact or largely intact
447 mature HIV-1 capsids (Figure 7f and supplementary movie 1). Such structures were
448 recently identified in nuclei of infected cells by CLEM using fluorescently labeled HIV-
449 1 IN as an indirect marker for subviral structures (Muller et al., 2021; Zila et al., 2021a)
450 and were interpreted as capsid shells solely based on their morphology. Here, we
451 demonstrated that these capsid-resembling structures co-localize with nuclear foci
452 comprising a high number of click labeled CA molecules. We thereby provide direct
453 evidence that the cone-shaped objects are complete or largely complete HIV-1 capsids
454 that have entered the nucleus presumably through the NPC of infected and cell cycle
455 arrested cells.

456

457 **Discussion**

458 Here, we present a direct labeling approach for HIV-1 CA that yields infectious and
459 morphologically mature viral particles. The minimally invasive GCE/click labeling
460 approach used here represents an ideal strategy for the versatile labeling of genetically
461 fragile viral capsid proteins in principle, but its potential for virus imaging has not been
462 exploited so far. The combination of GCE and subsequent functionalization of a viral
463 capsid protein by click chemistry has previously only been applied to the non-
464 enveloped adeno-associated virus (AAV) (e.g., (Kelemen et al., 2018; Zhang et al.,
465 2018). However, the capsid of AAV, unlike HIV-1 CA, can also tolerate peptide
466 insertions and larger modifications (Borner et al., 2020; Chandran et al., 2017; Feiner
467 et al., 2019; Varadi et al., 2012). Here, we demonstrate that GCE in conjunction with
468 click labeling can also be applied to an enveloped virus with a highly multifunctional
469 and genetically fragile capsid protein that needs to form a closed fullerene lattice to be
470 infectious. We found that HIV-1 CA tolerates chemical modification of the exposed
471 amino acid residue A14. This position is located close to the central, dynamic pore in
472 the CA hexamer lined by positively charged R18 and K25 rings (Jacques et al., 2016).
473 Replacement of A14 and E45 by cysteine residues for disulfide cross-linking CA
474 subunits was previously shown to allow CA hexamer assembly and was used to study
475 the capsid hexamer structure (Pornillos et al., 2009). This mutant retained binding to
476 host cell proteins Nup153 and CPSF6, as well as to dNTPs and PF74 (Jacques et al.,

477 2016; Price et al., 2014), consistent with functional replacement of A14 by a non-
478 natural CpK residue in the current study.

479 All previously described genetic tagging strategies for HIV-1 CA (Burdick et al., 2020;
480 Campbell et al., 2008; Pereira et al., 2011; Zurnic Bonisch et al., 2020) required
481 complementation with a molar excess of wt protein or virus. Since the mature HIV-1
482 capsid is assembled from approximately half of the ~2,500 CA molecules packaged in
483 the virion (Briggs et al., 2004; Lanman et al., 2004), it cannot be ascertained in this
484 case whether the subset of genetically tagged CA molecules is an integral part of the
485 mature capsid lattice. Conceivably, tagged or modified CA molecules may be excluded
486 from the mature capsid shell or may be irregularly inserted. Signal intensity changes
487 of CA fusion proteins in early HIV-1 replication may thus also depend on the relative
488 incorporation of these proteins into the mature capsid lattice. In contrast, we found that
489 the strategy described here allowed genetic labeling of HIV-1 CA in the proviral context
490 and retaining almost full infectivity in the absence of wild-type complementation.

491 The detection of a label covalently attached to CA is independent of cellular context,
492 sample treatment, or exposure of CA epitopes. Thereby, the method overcomes
493 limitations of IF detection that had previously resulted in different conclusions regarding
494 the presence of CA on subviral complexes. The use of synthetic dye molecules also
495 renders the labeling strategy compatible with a wide range of fluorescence imaging
496 approaches, including live-cell microscopy, correlative imaging and super-resolution
497 fluorescence microscopy techniques (Wang et al., 2019).

498 Our approach allowed for direct, quantitative analysis of CA-containing objects and CA
499 amounts associated with viral complexes in microscopic images of infected cells. While
500 time-lapse experiments showed some delay in nuclear import kinetics for labeled
501 capsid-like objects, the infectivity of highly labeled preparations was reduced by only
502 twofold, and the number of nuclear objects reached was similar to that detected in cells
503 infected with wt virus. Thus, site-specific introduction of a synthetic fluorophore can be
504 compatible with capsid functionality in HIV-1 post-entry processes. The delay in
505 nuclear accumulation appears to be mainly caused by slower trafficking through the
506 NPC, possibly due to the additional mass of the ncAA and label, given that the
507 unmodified HIV-1 capsid already approaches the size limit even of dilated NPCs (Zila
508 et al., 2021a). Another, not mutually exclusive, possibility is that ncAA incorporation

509 and/or the attached SiR dye affects pliability of the capsid structure that might be
510 required for efficient and fast passage through the NPC.

511 CA amounts approximately corresponding to the full complement of a mature capsid
512 were found to be associated with cytoplasmic post-fusion objects and with subviral
513 complexes in nuclei of a HeLa-derived cell line and primary human $CD4^+$ T cells, also
514 upon inhibition of cell division by aphidicolin treatment. By applying correlative imaging,
515 we provide direct evidence that nuclear complexes positive for directly labeled CA
516 indeed represent HIV-1 capsids or capsid-like remnants. Taken together, these results
517 argue against (partial) capsid uncoating prior to entering the nucleoplasm, as had been
518 concluded earlier based on low or lacking CA IF signals associated with nuclear
519 subviral complexes in certain cell types (e.g. (Burdick et al., 2017; Hulme et al., 2015;
520 Peng et al., 2014; Zila et al., 2019), or based on the loss of the fluorescently labeled
521 capsid binding protein CypA at the nuclear envelope (Francis et al., 2020a; Francis et
522 al., 2016; Francis and Melikyan, 2018). The apparent discrepancy between these
523 previous IF results and data from direct CA quantification may be explained by
524 differential accessibility of CA epitopes under different IF conditions. The indirect label
525 CypA, on the other hand, might be displaced from capsids at the nuclear pore, possibly
526 by competition between fluorescent CypA and the outer NPC protein Nup358, which
527 also carries a binding site for the CypA binding loop of CA (Schaller et al., 2011). Our
528 data suggest nuclear capsid uncoating in a model cell line, as well as in primary T cells,
529 in agreement with recent findings from us and others, which indicated that the nuclear
530 pore channel is wider than previously assumed, allowing HIV-1 capsids to pass the
531 intact NPC (Zila et al., 2021a), and that HIV-1 uncoating occurs after nuclear import
532 (Burdick et al., 2020; Dharan et al., 2020; Li et al., 2021; Muller et al., 2022; Selyutina
533 et al., 2020) , apparently by separation of the viral genome from a broken capsid
534 remnant (Muller et al., 2021).

535 Small clusters of CA positive objects were detected by STED nanoscopy in nuclei of
536 TZM-bl cells and T cells, consistent with the reported detection of nuclear clusters
537 containing multiple HIV-1 replication complexes (Francis et al., 2020b), multiple viral
538 genomes (Rensen et al., 2021), or even several intact or partly intact capsid-like
539 structures (Muller et al., 2021) in various cell types. Our analyses revealed that the
540 observed clustering is dependent on the amount of virus used for infection. Most
541 nuclear signals represented single capsids at a lower MOI, whereas frequent clustering
542 was observed at high MOI. This observation suggests that capsids enter the nucleus

543 individually, but traffic via a limited number of routes and accumulate at defined sites
544 of uncoating. This raises the question whether HIV-1 capsids use a 'specialized' subset
545 of nuclear pores for nuclear entry; the answer would not only be relevant in the context
546 of HIV-1 replication, but also with respect to an understanding of the nuclear import
547 process. Intracellular Nup levels and presumably NPC composition have been
548 reported to influence HIV-1 replication (Kane et al., 2018), but compositional and
549 structural variability of NPCs between different cell types, or within an individual cell, is
550 incompletely understood (reviewed in (Knockenhauer and Schwartz, 2016). The route,
551 mechanism and functional consequences of intranuclear trafficking of HIV-1
552 complexes also warrant further analysis. Growing evidence from recent studies
553 suggests that incoming viral replication complexes accumulate at nuclear speckles in
554 a CA and CPSF6-dependent manner, and that reverse transcription may only be
555 completed near the site of integration (Burdick et al., 2020; Francis et al., 2020a;
556 Rensen et al., 2021; Selyutina et al., 2020). Combining the direct CA labeling described
557 here with the recently developed fluorescence detection of the reverse transcribed
558 genome (Blanco-Rodriguez et al., 2020; Muller et al., 2021) will provide us with the
559 possibility to study the uncoating process in more detail using a combination of
560 confocal imaging, nanoscopy and correlative imaging.

561 The direct labeling approach also allowed us to investigate the effect of the capsid
562 inhibitor PF74 (Blair et al., 2010), whose detailed mode of action is still under
563 investigation. We found that displacement of CPSF6 from nuclear subviral structures
564 was not accompanied by a loss of CA signal. This finding disagrees with the recently
565 reported rapid CA dissociation from nuclear complexes upon PF74 addition, that was
566 based on imaging of HIV-1 particles containing eGFP-CA complemented by a molar
567 excess of wt CA (Burdick et al., 2020). The apparent discrepancy may suggest that the
568 subset of eGFP-tagged CA molecules is not an integral part of the mature capsid
569 lattice, resulting in premature loss of the labeled molecules. Our findings are in line
570 with the observation of other recent studies where PF74 treatment did not lead to a
571 loss of the CA IF signal on nuclear complexes but rather enhanced immunostaining
572 efficiency (Francis et al., 2020b; Muller et al., 2021) and with *in vitro* findings that
573 indicated breach of lattice integrity by PF74, but stabilization of the remaining lattice
574 (Marquez et al., 2019; Rankovic et al., 2018).

575 In conclusion, direct click labeling of HIV-1 CA is a versatile approach that substantially
576 expands the possibilities to study the early events in HIV-1 replication with high

577 temporal and/or spatial resolution using advanced fluorescence microscopy methods.
578 Application for HIV-1 CA demonstrated its usefulness for genetically fragile structural
579 proteins and provided direct proof that the capsid stays largely intact upon passage of
580 the subviral complex into the nucleus. Furthermore, it directly identified nuclear capsid-
581 like structures that morphologically resembled the virion capsid by CLEM-ET. The
582 variety of synthetic fluorophores which can be combined with GCE and click labeling
583 enables rapid adaptation of the approach to microscopic single-molecule techniques
584 such as STORM (Rust et al., 2006) and MINFLUX (Balzarotti et al., 2017). It can also
585 be combined with labeling of proteins of the viral replication complex and of the viral
586 genome, which is a subject of ongoing studies. Beyond fluorescence imaging, CA
587 modification by GCE offers possibilities for site-specific incorporation of other
588 functionalized ncAAs, e.g., benzoyl-phenylalanine (Coin, 2018) for photo-crosslinking,
589 together with pulldown experiments for the detection of capsid-host protein
590 interactions. The fact that the combination of GCE and click chemistry could
591 successfully be applied to a notoriously genetically fragile capsid protein of an
592 enveloped virus opens the perspective that this strategy may also advance and expand
593 fluorescence labeling of a broad range of other viruses.

594

595 **Acknowledgements**

596 We acknowledge microscopy support from the Infectious Diseases Imaging Platform
597 (IDIP) at the Center for Integrative Infectious Disease Research, Heidelberg. We thank
598 Eyal Arbely (The National Institute for Biotechnology in the Negev, Beer-Sheva, Israel)
599 for providing pEA168. pNESPylRS-eRF1dn-tRNA was kindly provided by Volkan Sakin
600 and Anna-Lena Schäfer (University Hospital Heidelberg, Heidelberg, Germany).

601 This work was funded in part by the Deutsche Forschungsgemeinschaft (DFG;
602 German Research Foundation), Projektnummer 240245660, SFB 1129 project 6
603 (B.M.) and project 5 (H.G.K.) and from DZIF (to H.G.K. and V.L.).

604

605 **Materials and Methods**

606 **Plasmids**

607 Plasmids were cloned using standard molecular biology techniques and verified by
608 commercial Sanger sequencing (Eurofins Genomics). PCR was performed using Q5

609 High-Fidelity DNA Polymerase (New England Biolabs) or Phusion DNA Polymerase
610 (New England Biolabs) according to the manufacturer's instructions using primers
611 purchased from Eurofins Genomics. Plasmid amplification was carried out in *E. coli*
612 Stbl2 (Thermo Fisher Scientific) cells.

613 HIV-1 plasmids were based on the proviral plasmid pNLC4-3 (Bohne and Krausslich,
614 2004) that expresses the authentic genomic RNA from HIV-1_{NL4-3} (Adachi et al., 1986)
615 under the control of the cytomegalovirus promoter. To avoid unwanted ncAA
616 incorporation into the virion component Vpr, the amber stop codon of the *vpr* ORF of
617 pNLC4-3 was mutated into an opal stop codon (TGA) via site-directed mutagenesis.
618 See primer list for sequences of primers used. PCR1 (primers Vpr_{TGA} a and Vpr_{TGA} b)
619 and PCR2 (primers Vpr_{TGA} c and Vpr_{TGA} d) were performed in parallel to generate two
620 overlapping single stranded PCR products. Using a combination of both products of
621 these reactions as new templates, PCR3 with primers Vpr_{TGA} a and Vpr_{TGA} d resulted
622 in PCR fragments comprising the respective mutation. These fragments were cloned
623 into pNLC4-3 using unique PflMI/NheI restriction sites, resulting in pNLC4-3*. Virus
624 produced from this plasmid was termed HIV-1*.

625 To allow for site-specific GCE, the codon for amino acid A14 of CA was mutated into
626 TAG via overlap PCR. PCR1 (primers $CA14_{BssHII}$ fwd 1, $CA14_{TAG}$ rev 1) and PCR2
627 (primers $CA14_{TAG}$ fwd 2, $CA14_{ApaI}$ rev 2) were performed in parallel to generate two
628 overlapping single-stranded PCR products. PCR3 with primers $CA14_{BssHII}$ fwd 1 and
629 $CA14_{ApaI}$ rev 2 result in the PCR fragment comprising the mutation, which was
630 subcloned into pNLC4-3* using unique BssHII/ApaI restriction sites, resulting in
631 pNLC4-3*$CA14^{TAG}$ (HIV-1*$CA14^{TAG}$).

632 Plasmid pNESPylRS-eRF1dn-tRNA (Schifferdecker, Sakin et al., in preparation) is
633 based on pEA168 (Cohen and Arbely, 2016), kindly provided by Eyal Arbely, Ben-
634 Gurion University of the Negev, Israel), a eukaryotic vector that comprises expression
635 cassettes for two proteins and four tRNA molecules. The coding sequence for a
636 modified pyrrolysine tRNA synthetase was cloned from plasmid $tRNA^{Pyl}$/$NESPylRS^{AF}$
637 (Nikic et al., 2016) into the CMV promoter driven expression cassette of pEA168 using
638 HindIII/XbaI restriction sites, resulting in plasmid pEA168-CMV-aaRS-4xU6tRNA. A
639 PCR fragment encoding a dominant version of the eukaryotic release factor 1
640 (eRF1(E55D)) amplified from plasmid peRF1-E55D (Schmied et al., 2014) was
641 subsequently inserted into an expression cassette driven by the EF1 promotor into

642 pEA168-CMV-aaRS-4xU6tRNA using KpnI/MluI restriction sites, yielding pNESPylRS-
643 eRF1dn-tRNA.

644

645 Table 1 Primers

primer	sequence
Vpr_{TGA} a	ctggcatttgggtcagggagtc
Vpr_{TGA} b	cagggctctagttcaggatctactggctc
Vpr_{TGA} c	gagccagtagatcctgaactagagccctg
Vpr_{TGA} d	gttctcttaatttgctagc
CA $A14_{BssHII}$ fwd 1	cttgctgaagcgcgca
CA $A14_{TAG}$ rev 1	agttctaggtgatatctactgatgtaccatttg
CA $A14_{TAG}$ fwd 2	caaatggtacatcagtagatatcacctagaact
CA $A14_{ApaI}$ rev 2	gccctgcaatttttggctatgtg

646

647 **Cell culture**

648 HEK293T (Pear et al., 1993) and HeLa TZM-bl indicator cells (Wei et al., 2002) were
649 maintained in Dulbecco´s Modified Eagle´s medium (Thermo Fisher Scientific)
650 supplemented with 100 U/ml penicillin, 100 µg/ml streptomycin (PAN Biotech) and 10%
651 fetal calf serum (FCS; Sigma Aldrich). Both cell lines were regularly monitored for
652 mycoplasma contamination using the MycoAlert mycoplasma detection kit (Lonza
653 Rockland). Primary CD4+ T cells were cultured in RPMI 1640 containing L-glutamine
654 supplemented with 100 U/ml penicillin, 100 µg/ml streptomycin (PAN Biotech), 10%
655 heat-inactivated FCS, and 5% human AB serum (Sigma Aldrich).

656

657 **Isolation of primary cells**

658 Primary human CD4+ T cells were isolated from buffy coats obtained from healthy and
659 anonymous blood donors at the Heidelberg University Hospital Blood Bank following
660 the regulations of the local ethics committee. CD4+ T cells were isolated using
661 EasySep™ Direct Human T Cell Isolation Kit (Stemcell technologies) according to the
662 manufacturer's instructions and activated by incubation in the presence of 100 U/ml IL-
663 2 (Sigma Aldrich) and T Cell TransAct™ human (Miltenyi Biotec) for 72 h.

664

665 **Virus particle production**

666 HEK293T cells were seeded in T175 tissue culture flasks the day before (~15 Mio.
667 cells) or a 6-well plate (4x10^5 cells/well) and transfected using calcium phosphate
668 precipitation according to standard procedures (~80% confluency). Cells were co-
669 transfected with 50 µg/flask or 3 µg/well total DNA of pNLC4-3* (HIV-1*) or pNLC4-
670 3*CA14^{TAG} (HIV-1*CA14^{TAG}) and plasmid pNESPylRS-eRF1dn-tRNA in a molar ratio
671 of 2.22:1. At 6 h p.t., medium was removed, and fresh complete DMEM containing a
672 final concentration of 500 µM CpK (SiChem; stock solution of 100 mM was pre-diluted
673 1:4 in 1M HEPES shortly before use), and 100 µM ascorbic acid (Sigma Aldrich; stock
674 solution 10 mM) was added. At 48 h p.t., the tissue culture supernatant was harvested
675 and filtered through 0.45 µm nitrocellulose filters. For labeling the CA protein, 250 nM
676 Tetrazine-SiR (Spirochrome; stock solution 1 mM) was added to the filtered
677 supernatant, and samples were incubated at 37°C for 30 min. Particles were then
678 concentrated by ultracentrifugation through a 20% (w/v) sucrose cushion at 28,000
679 rpm using a Beckman TLA-100 fixed angle-rotor (Beckman Coulter) for 90 min or for
680 the 6-well format at 44,000 rpm using a Beckman TLA-55 fixed angle-rotor (Beckman
681 Coulter) for 45 min at 4°C. Pellets were gently resuspended in phosphate-buffered
682 saline (PBS) containing 10% FCS and 10 mM HEPES (pH 7.5) and stored in 5 µl
683 aliquots at -80°C.

684

685 **Immunoblotting and In-gel fluorescence**

686 Virus samples were mixed 1:10 with SDS sample buffer (150 mM Tris HCl, pH 6.8, 6%
687 (w/v) SDS, 30% Glycerin, 0.06% bromophenol blue, 20% β -Mercaptoethanol) and
688 boiled at 95°C for 15 min. 10 µl HIV-1* and 40 µl HIV-1*CA^{SiR} lysates were subjected
689 to SDS-PAGE (15 %; acrylamide:bisacrylamide 200:1). Cell lysates were generated
690 from transfected HEK293T cells. At 40 h p.t., cells were washed with PBS, trypsinized
691 and resuspended in PBS. 1 ml of cell suspension was mixed with 300 µl SDS sample
692 buffer and boiled at 95°C for 15 min. 10 µl cell lysate was subjected to SDS-PAGE.
693 Proteins were transferred to a nitrocellulose membrane (Millipore) by semi-dry blotting
694 for 1 h at 0.8 mA/cm^2. Antigens were stained with the indicated antisera in PBS/0.5%
695 bovine serum albumin (BSA) (sheep αCA, polyclonal 1:5,000 (in-house); rabbit αMA,
696 polyclonal 1:1,000 (in-house); rabbit αRT, polyclonal, 1:1,000 (in-house), followed by

697 staining with corresponding secondary antibodies IRDye^{TM} in PBS / 0.5% BSA (anti-
698 sheep 680CW (1:10,000); Rockland, or anti-rabbit 800CW (1:10,000); Li-COR
699 Biosciences). Detection was performed using a Li-COR Odyssey CLx infrared scanner
700 (Li-COR Biosciences) according to manufacturer's instructions. CA quantification was
701 performed with ImageStudio LITE software (Li-COR Biosciences) via intensity
702 measurements of CA bands and a serial dilution of recombinant purified CA standard
703 (2.5 ng/µl; in-house) on the same membrane. For in-gel fluorescence, the acrylamide
704 gels were directly scanned using a Li-COR Odyssey CLx infrared scanner (Li-COR
705 Biosciences) set at an emission wavelength of 700 nm.

706

707 **Infectivity assays**

708 Virus amounts were quantified via SYBR Green based Product Enhanced Reverse
709 Transcription assay (SG-PERT; (Pizzato et al., 2009)). To determine relative infectivity
710 of HIV-1* particles in a luciferase assay, 5,000 TZM-bl cells were seeded in 90 µl
711 DMEM in a 96-well plate. On the following day, infection was performed 10 µl of serial
712 9-fold dilution of supernatant from virus producing HEK293T cells transfected with
713 pNLC4-3 or pNLC4-3*. At 48 h p.i., cells were lysed by adding 100 µl Steady-Glo
714 luciferase reagent (Promega). After 10 min, 80 µl of the lysed cell solution was
715 transferred into a white 96-well plate and an Infinite 200 PRO plate reader (TECAN)
716 was used to measure luminescence. Uninfected cells were used as a negative control.

717 To determine the effect of incorporating CpK and Tet-SiR labeling on virus infectivity,
718 HIV-1* and HIV-1*CA14^{SiR} viral particles (normalized by RT activity) were titrated on
719 TZM-bl cells seeded in 15-well ibidi µ-Slide angiogenesis dishes. At 6 h p.i. 50 µM T-
720 20 (Enfuvirtide; Roche; stock solution 20 mM) was added to prevent second-round
721 infection. Infection rates were scored at 48 h p.i.. For this, cells were fixed in 4%
722 paraformaldehyde (PFA; Electron Microscopy Sciences; stock solution 16%) for 15
723 min, followed by 20 min incubation in PBS/0.5% (v/v) Triton X-100 at room
724 temperature. Immunostaining was performed using an in-house polyclonal rabbit
725 antiserum raised against recombinant HIV-1 MA (1:1,000; in-house) in PBS/0.5% BSA)
726 1 h at room temperature. Secondary antibody Alexa Fluor 488 donkey anti-rabbit
727 (1:1,000; Thermo Fisher Scientific) in PBS/0.5% BSA was added for 45 min at room
728 temperature. Samples were imaged by SDCM. The mean intensity of the 488 channel
729 (MA IF) was quantified in the non-infected samples imaged in parallel and subtracted

730 as background in each image. The proportion of IF-positive cells was counted in 12
731 randomly selected fields of view using Fiji (Schindelin et al., 2012). To determine the
732 infectivity of virus particle preparations, the number of infected cells per well was
733 calculated by multiplying the percentage of infected cells detected with the number of
734 cells per well (double of seeded cell number the day before). Division by the volume of
735 virus suspension used for infection yielded the number of infectious units (IU) / ml.

736

737 **Fixation and immunofluorescence staining of infected cells**

738 3.33×10^3 TZM-bl cells were seeded into 15-well µ-Slides angiogenesis dishes (ibidi;
739 cat. 81507) the day before infection. Infection at 37°C was performed with an MOI ~0.8
740 for 6,9,12 or 18 h. Subsequently, cells were incubated for 1 h with 15 µM PF74 (Sigma
741 Aldrich; stock solution 10 mM in DMSO) in DMEM to allow for efficient detection of
742 nuclear CA by IF (Muller et al., 2021). Samples were washed with PBS, fixed in 4%
743 PFA for 15 min and permeabilized with PBS/0.5% (v/v) Triton-X100 for 20 min, and
744 washed again with PBS. Cells were extracted using ice-cold 100% methanol for 10
745 min. Afterward, samples were blocked with PBS/2.5% BSA for 15 min, followed by
746 incubation with primary antibodies (rabbit αCA, polyclonal 1:1000 (in-house); rabbit
747 αCPSF6, polyclonal 1: (Atlas Antibodies, cat. #HPA039973); mouse αhLamin A/C,
748 monoclonal 1:100 (Santa Cruz Biotech., cat. #sc-7292); mouse αhLaminB1,
749 monoclonal 1:100 (Santa Cruz Biotech., cat. #sc-365962)) in PBS/0.5% BSA for 1 h at
750 room temperature. After washing three times with PBS, secondary antibodies (Alexa
751 Fluor 405, 488, 568, goat/donkey, polyclonal 1:1,000 (Thermo Fisher Scientific))
752 diluted in PBS/0.5% BSA were added for 45 min at room temperature. Samples were
753 washed and stored in PBS at 4°C. For infection of primary $CD4^+$ T cells, 20,000 cells
754 were infected with HIV-1* or HIV-1*$CA14^{SiR}$ in a 96-well v-bottom microplate (Greiner
755 Bio-one, cat. #650161) in a volume of 40 µl RPMI and transferred at 22 h p.i. onto a
756 PEI-coated 15-well µ-Slide angiogenesis dishes (ibidi). Cells were allowed to adhere
757 for 1 h at 37°C, and PF74 diluted in fresh growth medium was added to a final
758 concentration of 15 µM. Extraction, fixation, and immunostaining were performed after
759 1 h at 37°C as described above. For the detection of endosome-associated particles,
760 2 µM mCLING ATTO488 (Synaptic Systems; stock 50 µM) was added to TZM-bl cells
761 seeded in 15-well µ-Slides Angiogenesis and incubated at 16°C for 30 min.
762 Subsequently, the fluorescent probe was removed, HIV-1*$CA14^{SiR}$ particles were

763 added in fresh growth medium, and cells were incubated for an additional 3 h at 37°C
764 (MOI~0.8). Cells were fixed for 90 min at room temperature in 4% PFA and 0.2%
765 glutaraldehyde to ensure retention of mCLING at cellular membranes. Nuclei were
766 stained with 5 µg/ml Hoechst (Merck) in PBS for 30 min.

767

768 **Cell viability assay**

769 To test the effect of mCLING ATTO488 (Synaptic Systems) staining on cell viability,
770 TZM-bl cells were seeded into a 96-well plate ($5x10^3$ cells/well; flat bottom Greiner Bio-
771 one) the day before and incubated in medium supplemented with the indicated
772 concentration of mCLING ATTO488 for 30 min at 16°C. After staining, cells were
773 trypsinized, stained with Trypan blue using standard procedures and analyzed with a
774 TC20^{TM} Automated Cell Counter (BioRad).

775

776 **Labeling efficiency of immobilized particles**

777 15-well µ-Slide angiogenesis dishes (ibidi) were coated with 30µl/well
778 polyethyleneimine (PEI; 1mg/ml) for 30 min at room temperature and washed with
779 PBS. Pre-labeled HIV-1* and HIV-1*CA14^{SiR} particles were incubated in PBS on PEI-
780 coated microscopy slides for 1 h at 37°C. Subsequently, samples were washed with
781 PBS, fixed in 4% PFA for 15 min and permeabilized with PBS/0.05% (v/v) Triton X-100
782 for 20 min at room temperature. Immobilized particles were blocked with PBS/2.5%
783 BSA for 15 min and polyclonal rabbit antiserum raised against recombinant HIV-1 CA
784 protein (in-house) was added (1:1,000 in PBS/0.5% BSA for 1 h at room temperature).
785 After washing three times with PBS, secondary antibody Alexa Fluor 488 donkey anti-
786 rabbit (Thermo Fisher Scientific) 1:1,000 in PBS/0.5% BSA was added for 45 min at
787 room temperature. Samples were washed and stored in PBS at 4°C.

788

789 **Confocal microscopy (SDCM)**

790 Multichannel z-series with a z-spacing of 200 nm, spanning the whole cell volume (3D),
791 were acquired using a PerkinElmer Ultra VIEW VoX 3D spinning disk confocal
792 microscope (SDCM; Perkin Elmer). A 60x oil immersion objective (numeric aperture
793 [NA] 1.49; Perkin Elmer) was used for imaging of TZM-bl cells or 100x oil immersion

794 objective ([NA] 1.49; Perkin Elmer) for primary CD4+ T cells and immobilized particles.
795 Images were recorded in the 405-, 488-, 561-, and 640 nm channels.

796

797 **STED microscopy**

798 STED nanoscopy was performed using a λ = 775 nm STED system (Abberior
799 Instruments GmbH) equipped with a 100x oil immersion objective (NA 1.4; Olympus
800 UPlanSApo). STED images were acquired using the 640 nm excitation laser lines while
801 the 488 and 590 laser line was acquired in confocal mode only. Nominal STED laser
802 power was set to 20% of the maximal power (1250 mW) with pixel dwell time of 10 µs
803 and 15 nm pixel size. STED images were deconvolved using the software Imspector
804 (Abberior Instruments GmbH) and Huygens Professional Deconvolution (Scientific
805 Volume Imaging).

806

807 **Electron microscopy**

808 HEK293T cells (4×10^5) were seeded in a glass coverslip-bottom petri dish (MatTek,
809 MA, USA), cultured for 16 h at 37°C and then co-transfected with pNLC4-3*CA14^{TAG}
810 and pNESPylRS-eRF1dn-tRNA by using calcium phosphate precipitation. At 6 h p.t.,
811 medium was removed and fresh complete DMEM containing a final concentration of
812 500 µM CpK (SiChem; stock solution 100 mM was pre-diluted 1:4 in 1M HEPES shortly
813 before use), and 100 µM ascorbic acid (Sigma Aldrich; stock solution 10 mM) was
814 added. At 44 h p.t., cells were fixed with pre-warmed 2% formaldehyde + 2.5%
815 glutaraldehyde in 0.1 M cacodylate buffer (pH 7.4) for 1.5 h at room temperature, then
816 washed in 0.1 M cacodylate buffer and post-fixed with 2% osmium tetroxide (Electron
817 Microscopy Sciences) for a 1 h on ice. Cells were subsequently dehydrated through
818 an increasing cold ethanol series (30, 50, 70, 80, 90, and 100%; on ice) and two
819 anhydrous acetone series (at room temperature). The coverslip with cells was then
820 removed from the dish, and cells were flat embedded in Epon resin. 70-nm thin
821 sections were cut with an ultramicrotome (Leica EM UC6), collected on formvar-coated
822 100-mesh copper EM grids (Electron Microscopy Sciences) and stained with a 3%
823 uranyl acetate in 70% MetOH (10 min), and lead citrate (7 min). Cells sections were
824 observed with a JEOL JEM-1400 electron microscope operating at 80 kV (Jeol Ltd.),
825 equipped with a bottom-mounted 4K by 4K pixel digital camera (TemCam F416; TVIPS
826 GmbH).

827

828 **CLEM and electron tomography**

829 SupT1 cells were distributed in a 96-well plate (2x10^5 cells/well; U-bottom; Greiner Bio-
830 one, 650180) and pre-incubated for 16 h with 1 µm aphidicolin (APC; Merck). Cells
831 were pelleted (200 x g, 3 min) and resuspended in complete RPMI medium containing
832 HIV-1*CA14^{SIR} particles (MOI~0.4). Cells were incubated with viral particles for 120
833 min at 16°C to adsorb the virus and synchronize virus entry. Samples were then
834 processed for CLEM and ET as described previously (Zila et al., 2021a). In brief, cells
835 were transferred to glass-bottomed microwell of a MatTek dish (MatTek) containing
836 carbon-coated and retronectin-coated sapphire discs (Engineering Office M.
837 Wohlwend). Samples were high pressure frozen, and sapphire discs were then
838 transferred from liquid nitrogen to the freeze-substitution (FS) medium (0.1% uranyl
839 acetate, 2.3% methanol and 2% H_2O in acetone) tempered at -90°C. Samples were
840 FS-processed and embedded in Lowicryl HM20 resin (Polysciences) according to a
841 modified protocol of Kukulski et al. (Kukulski et al., 2011). For CLEM-ET, thick resin
842 sections (250 nm) were cut and placed on a slot (1 × 2 mm) EM copper grids covered
843 with a formvar film (Electron Microscopy Sciences, FF2010-Cu). Grids were decorated
844 with fiducial marker and stained with Hoechst to visualize nuclear regions. Light
845 microscopy Z stacks of sections were acquired by PerkinElmer UltraVIEW VoX 3D
846 Spinning-disc Confocal Microscope (Perkin Elmer) using a 100 × oil immersion
847 objective (NA 1.49; Nikon), with a *z*-spacing of 200 nm and excitation with the 405-,
848 488-, 561- and 633-nm laser line. Acquired z stacks were visually examined using Fiji
849 software (Schindelin et al., 2012) and intracellular CA(SiR) positive signals were
850 identified. EM grids were decorated with 15 nm protein-A gold particles for tomogram
851 alignment and stained with uranyl acetate and lead citrate. Grids were loaded to a
852 Tecnai TF20 (FEI) electron microscope (operated at 200 kV) equipped with a field
853 emission gun and a 4K by 4K pixel Eagle CCD camera (FEI). Positions of CA(SiR)
854 signals were pre-correlated with imported SDCM images in SerialEM as described
855 previously (Schorb et al., 2017). Single-axis electron tomograms were carried out.
856 Tomographic tilt ranges were typically from –60° to 60° with an angular increment of
857 1°. The pixel size was 1.13 nm. Alignments and 3D reconstructions of tomograms were
858 done with IMOD software (Kremer et al., 1996). Post-correlation was performed using
859 eC-CLEM plugin in Icy software (de Chaumont et al., 2012).

860

861 **Image analysis**

862 Microscopy images were screened and filtered in Fiji/ImageJ (Schindelin et al., 2012)
863 with a mean filter and background subtraction. Infected cells were quantified in Fiji via
864 segmentation and counting of nuclei and the cell counter to manually quantify the
865 number of positive cells. To determine labeling efficiency of click labeled particles,
866 CA(SiR) intensities of detected immobilized particles based on CA(IF) were quantified
867 using the spot detector of the software Icy (de Chaumont et al., 2012). Five ROIs
868 without particles were measured, and mean intensity in the SiR channel was
869 subtracted as background. The threshold was set to t = 1,000 a.u.. CA(IF) detected
870 spots with intensities above the threshold were classified as CA(SiR) positive.

871 To analyze particle distribution and intensity measurements throughout the entire
872 volume of cells, z-image series were reconstructed in 3D space using Imaris 9.2
873 software (Bitplane AG). Individual HIV-1 CA(IF) objects were automatically detected
874 using the spot detector Imaris module, which created for each fluorescent signal a 3D
875 ellipsoid object with 300 nm estimated diameter in *x-y* dimensions and 600 nm in *z*.
876 The local background of each individual spot was subtracted automatically.
877 Subsequently, the mean signal intensity in the CA(SiR) channel was quantitated within
878 all objects. The threshold for SiR intensity was set to t = 7,000 a.u. and adjusted
879 manually for each image by visual inspection. Spots detected in SiR-clusters were
880 excluded. Nuclear objects were manually identified based on the lamin A/C staining.
881 NE-associated objects were classified based on lamin A/C intensities. Every image
882 was manually inspected and a threshold for NE-associated objects was set in the range
883 of 6,300-9,100 a.u.. All other particles were classified as PM/cytoplasm (= in the
884 cytoplasm/at plasma membrane).

885 To identify post-fusion cores by mCLING ATTO488 staining, CA SiR positive objects
886 were automatically detected using the spot detector Imaris module and the mCLING
887 ATTO488 mean signal intensity co-localizing with each object was quantitated.
888 Particles located outside of the cell, attached to the plasma membrane, or within
889 clusters of foci were excluded from the analysis. Detected objects with the lowest
890 mCLING ATTO488 intensities were individually inspected. Only particles showing a
891 distinct CA SiR focus lacking the mCLING ATTO488 signal were classified as mCLING
892 negative.

Fiji standard 'greyscale' lookup table (LUT) was used to visualize single channel images and 'Fire' for single channel STED images.

Data visualization and statistical analysis

Statistical significance was assessed using Prism v9.1.0 (GraphPad Software Inc). A two-tailed non-paired Mann-Whitney test (α = 0.05) was used to assess the statistical significance of non-parametric data. Data were plotted using Prism v9.1.0 or the Python statistical data visualization package seaborn v.0.10.0 (Waskom 2020) Graphs show mean/median with error bars as defined in the figure legends.

Competing financial interests: The authors declare no competing financial interests.

References

Adachi, A., Gendelman, H.E., Koenig, S., Folks, T., Willey, R., Rabson, A., and Martin, M.A. (1986). Production of acquired immunodeficiency syndrome-associated retrovirus in human and nonhuman cells transfected with an infectious molecular clone. Journal of virology *59*, 284-291.

Aiken, C., and Rousso, I. (2021). The HIV-1 capsid and reverse transcription. Retrovirology *18*, 29.

Balzarotti, F., Eilers, Y., Gwosch, K.C., Gynna, A.H., Westphal, V., Stefani, F.D., Elf, J., and Hell, S.W. (2017). Nanometer resolution imaging and tracking of fluorescent molecules with minimal photon fluxes. Science *355*, 606-612.

Bhattacharya, A., Alam, S.L., Fricke, T., Zadrozny, K., Sedzicki, J., Taylor, A.B., Demeler, B., Pornillos, O., Ganser-Pornillos, B.K., Diaz-Griffero, F.*, et al.* (2014). Structural basis of HIV-1 capsid recognition by PF74 and CPSF6. Proceedings of the National Academy of Sciences of the United States of America *111*, 18625-18630.

Blair, W.S., Pickford, C., Irving, S.L., Brown, D.G., Anderson, M., Bazin, R., Cao, J., Ciaramella, G., Isaacson, J., Jackson, L.*, et al.* (2010). HIV capsid is a tractable target for small molecule therapeutic intervention. PLoS pathogens *6*, e1001220.

Blanco-Rodriguez, G., Gazi, A., Monel, B., Frabetti, S., Scoca, V., Mueller, F., Schwartz, O., Krijnse-Locker, J., Charneau, P., and Di Nunzio, F. (2020). Remodeling of the Core Leads HIV-1 Preintegration Complex into the Nucleus of Human Lymphocytes. Journal of virology *94*.

929 Bohne, J., and Krausslich, H.G. (2004). Mutation of the major 5' splice site renders a CMV-
930 driven HIV-1 proviral clone Tat-dependent: connections between transcription and splicing.
931 FEBS letters *563*, 113-118.
932 Borner, K., Kienle, E., Huang, L.Y., Weinmann, J., Sacher, A., Bayer, P., Stullein, C.,
933 Fakhiri, J., Zimmermann, L., Westhaus, A.*, et al.* (2020). Pre-arrayed Pan-AAV Peptide
934 Display Libraries for Rapid Single-Round Screening. Molecular therapy : the journal of the
935 American Society of Gene Therapy *28*, 1016-1032.
936 Briggs, J.A., Simon, M.N., Gross, I., Krausslich, H.G., Fuller, S.D., Vogt, V.M., and Johnson,
937 M.C. (2004). The stoichiometry of Gag protein in HIV-1. Nature structural & molecular
938 biology *11*, 672-675.
939 Briggs, J.A., Wilk, T., Welker, R., Krausslich, H.G., and Fuller, S.D. (2003). Structural
940 organization of authentic, mature HIV-1 virions and cores. The EMBO journal *22*, 1707-
941 1715.
942 Burdick, R.C., Delviks-Frankenberry, K.A., Chen, J., Janaka, S.K., Sastri, J., Hu, W.S., and
943 Pathak, V.K. (2017). Dynamics and regulation of nuclear import and nuclear movements of
944 HIV-1 complexes. PLoS pathogens *13*, e1006570.
945 Burdick, R.C., Li, C., Munshi, M., Rawson, J.M.O., Nagashima, K., Hu, W.S., and Pathak,
946 V.K. (2020). HIV-1 uncoats in the nucleus near sites of integration. Proceedings of the
947 National Academy of Sciences of the United States of America *117*, 5486-5493.
948 Campbell, E.M., and Hope, T.J. (2015). HIV-1 capsid: the multifaceted key player in HIV-1
949 infection. Nature reviews Microbiology *13*, 471-483.
950 Campbell, E.M., Perez, O., Anderson, J.L., and Hope, T.J. (2008). Visualization of a
951 proteasome-independent intermediate during restriction of HIV-1 by rhesus TRIM5alpha. The
952 Journal of cell biology *180*, 549-561.
953 Carlson, L.A., Briggs, J.A., Glass, B., Riches, J.D., Simon, M.N., Johnson, M.C., Muller, B.,
954 Grunewald, K., and Krausslich, H.G. (2008). Three-dimensional analysis of budding sites and
955 released virus suggests a revised model for HIV-1 morphogenesis. Cell host & microbe *4*,
956 592-599.
957 Chandran, J.S., Sharp, P.S., Karyka, E., Aves-Cruzeiro, J., Coldicott, I., Castelli, L.,
958 Hautbergue, G., Collins, M.O., and Azzouz, M. (2017). Site Specific Modification of Adeno-
959 Associated Virus Enables Both Fluorescent Imaging of Viral Particles and Characterization of
960 the Capsid Interactome. Scientific reports *7*, 14766.
961 Cohen, S., and Arbely, E. (2016). Single-Plasmid-Based System for Efficient Noncanonical
962 Amino Acid Mutagenesis in Cultured Mammalian Cells. Chembiochem : a European journal
963 of chemical biology *17*, 1008-1011.
964 Coin, I. (2018). Application of non-canonical crosslinking amino acids to study protein-
965 protein interactions in live cells. Current opinion in chemical biology *46*, 156-163.
966 de Chaumont, F., Dallongeville, S., Chenouard, N., Herve, N., Pop, S., Provoost, T., Meas-
967 Yedid, V., Pankajakshan, P., Lecomte, T., Le Montagner, Y.*, et al.* (2012). Icy: an open
968 bioimage informatics platform for extended reproducible research. Nature methods *9*, 690-
969 696.
970 Dharan, A., Bachmann, N., Talley, S., Zwikelmaier, V., and Campbell, E.M. (2020). Nuclear
971 pore blockade reveals that HIV-1 completes reverse transcription and uncoating in the
972 nucleus. Nature microbiology *5*, 1088-1095.
973 Engelman, A.N. (2021). HIV Capsid and Integration Targeting. Viruses *13*.
974 Feiner, R.C., Teschner, J., Teschner, K.E., Radukic, M.T., Baumann, T., Hagen, S.,
975 Hannappel, Y., Biere, N., Anselmetti, D., Arndt, K.M.*, et al.* (2019). rAAV Engineering for
976 Capsid-Protein Enzyme Insertions and Mosaicism Reveals Resilience to Mutational,
977 Structural and Thermal Perturbations. International journal of molecular sciences *20*.

978 Francis, A.C., Marin, M., Prellberg, M.J., Palermino-Rowland, K., and Melikyan, G.B.
979 (2020a). HIV-1 Uncoating and Nuclear Import Precede the Completion of Reverse
980 Transcription in Cell Lines and in Primary Macrophages. Viruses *12*.
981 Francis, A.C., Marin, M., Shi, J., Aiken, C., and Melikyan, G.B. (2016). Time-Resolved
982 Imaging of Single HIV-1 Uncoating In Vitro and in Living Cells. PLoS pathogens *12*,
983 e1005709.
984 Francis, A.C., Marin, M., Singh, P.K., Achuthan, V., Prellberg, M.J., Palermino-Rowland, K.,
985 Lan, S., Tedbury, P.R., Sarafianos, S.G., Engelman, A.N.*, et al.* (2020b). HIV-1 replication
986 complexes accumulate in nuclear speckles and integrate into speckle-associated genomic
987 domains. Nature communications *11*, 3505.
988 Francis, A.C., and Melikyan, G.B. (2018). Single HIV-1 Imaging Reveals Progression of
989 Infection through CA-Dependent Steps of Docking at the Nuclear Pore, Uncoating, and
990 Nuclear Transport. Cell host & microbe *23*, 536-548 e536.
991 Hulme, A.E., Kelley, Z., Foley, D., and Hope, T.J. (2015). Complementary Assays Reveal a
992 Low Level of CA Associated with Viral Complexes in the Nuclei of HIV-1-Infected Cells.
993 Journal of virology *89*, 5350-5361.
994 Hulme, A.E., Perez, O., and Hope, T.J. (2011). Complementary assays reveal a relationship
995 between HIV-1 uncoating and reverse transcription. Proceedings of the National Academy of
996 Sciences of the United States of America *108*, 9975-9980.
997 Jacques, D.A., McEwan, W.A., Hilditch, L., Price, A.J., Towers, G.J., and James, L.C.
998 (2016). HIV-1 uses dynamic capsid pores to import nucleotides and fuel encapsidated DNA
999 synthesis. Nature *536*, 349-353.
1000 James, L.C. (2019). The HIV-1 Capsid: More than Just a Delivery Package. Advances in
1001 experimental medicine and biology *1215*, 69-83.
1002 Kane, M., Rebensburg, S.V., Takata, M.A., Zang, T.M., Yamashita, M., Kvaratskhelia, M.,
1003 and Bieniasz, P.D. (2018). Nuclear pore heterogeneity influences HIV-1 infection and the
1004 antiviral activity of MX2. eLife *7*.
1005 Kelemen, R.E., Erickson, S.B., and Chatterjee, A. (2018). Production and Chemoselective
1006 Modification of Adeno-Associated Virus Site-Specifically Incorporating an Unnatural Amino
1007 Acid Residue into Its Capsid. Methods in molecular biology *1728*, 313-326.
1008 Knockenhauer, K.E., and Schwartz, T.U. (2016). The Nuclear Pore Complex as a Flexible and
1009 Dynamic Gate. Cell *164*, 1162-1171.
1010 Kremer, J.R., Mastronarde, D.N., and McIntosh, J.R. (1996). Computer visualization of three-
1011 dimensional image data using IMOD. Journal of structural biology *116*, 71-76.
1012 Kukulski, W., Schorb, M., Welsch, S., Picco, A., Kaksonen, M., and Briggs, J.A. (2011).
1013 Correlated fluorescence and 3D electron microscopy with high sensitivity and spatial
1014 precision. The Journal of cell biology *192*, 111-119.
1015 Lang, K., and Chin, J.W. (2014). Cellular incorporation of unnatural amino acids and
1016 bioorthogonal labeling of proteins. Chemical reviews *114*, 4764-4806.
1017 Lanman, J., Lam, T.T., Emmett, M.R., Marshall, A.G., Sakalian, M., and Prevelige, P.E., Jr.
1018 (2004). Key interactions in HIV-1 maturation identified by hydrogen-deuterium exchange.
1019 Nature structural & molecular biology *11*, 676-677.
1020 Li, C., Burdick, R.C., Nagashima, K., Hu, W.S., and Pathak, V.K. (2021). HIV-1 cores retain
1021 their integrity until minutes before uncoating in the nucleus. Proceedings of the National
1022 Academy of Sciences of the United States of America *118*.
1023 Lukinavicius, G., Umezawa, K., Olivier, N., Honigmann, A., Yang, G., Plass, T., Mueller, V.,
1024 Reymond, L., Correa, I.R., Jr., Luo, Z.G.*, et al.* (2013). A near-infrared fluorophore for live-
1025 cell super-resolution microscopy of cellular proteins. Nature chemistry *5*, 132-139.
1026 Mamede, J.I., Cianci, G.C., Anderson, M.R., and Hope, T.J. (2017). Early cytoplasmic
1027 uncoating is associated with infectivity of HIV-1. Proceedings of the National Academy of
1028 Sciences of the United States of America *114*, E7169-E7178.

1029 Marquez, C.L., Lau, D., Walsh, J., Faysal, K.M.R., Parker, M.W., Turville, S.G., and
1030 Bocking, T. (2019). Fluorescence Microscopy Assay to Measure HIV-1 Capsid Uncoating
1031 Kinetics in vitro. Bio-protocol *9*, e3297.
1032 Marquez, C.L., Lau, D., Walsh, J., Shah, V., McGuinness, C., Wong, A., Aggarwal, A.,
1033 Parker, M.W., Jacques, D.A., Turville, S.*, et al.* (2018). Kinetics of HIV-1 capsid uncoating
1034 revealed by single-molecule analysis. eLife *7*.
1035 Matreyek, K.A., Yucel, S.S., Li, X., and Engelman, A. (2013). Nucleoporin NUP153
1036 phenylalanine-glycine motifs engage a common binding pocket within the HIV-1 capsid
1037 protein to mediate lentiviral infectivity. PLoS pathogens *9*, e1003693.
1038 Mattei, S., Schur, F.K., and Briggs, J.A. (2016). Retrovirus maturation-an extraordinary
1039 structural transformation. Current opinion in virology *18*, 27-35.
1040 Melikyan, G.B., Markosyan, R.M., Hemmati, H., Delmedico, M.K., Lambert, D.M., and
1041 Cohen, F.S. (2000). Evidence that the transition of HIV-1 gp41 into a six-helix bundle, not the
1042 bundle configuration, induces membrane fusion. The Journal of cell biology *151*, 413-423.
1043 Muller, B., Tessmer, U., Schubert, U., and Krausslich, H.G. (2000). Human
1044 immunodeficiency virus type 1 Vpr protein is incorporated into the virion in significantly
1045 smaller amounts than gag and is phosphorylated in infected cells. Journal of virology *74*,
1046 9727-9731.
1047 Muller, T.G., Sakin, V., and Muller, B. (2019). A Spotlight on Viruses-Application of Click
1048 Chemistry to Visualize Virus-Cell Interactions. Molecules *24*.
1049 Muller, T.G., Zila, V., Muller, B., and Krausslich, H.G. (2022). Nuclear Capsid Uncoating
1050 and Reverse Transcription of HIV-1. Annual review of virology.
1051 Muller, T.G., Zila, V., Peters, K., Schifferdecker, S., Stanic, M., Lucic, B., Laketa, V., Lusic,
1052 M., Muller, B., and Krausslich, H.G. (2021). HIV-1 uncoating by release of viral cDNA from
1053 capsid-like structures in the nucleus of infected cells. eLife *10*.
1054 Naghavi, M.H. (2021). HIV-1 capsid exploitation of the host microtubule cytoskeleton during
1055 early infection. Retrovirology *18*, 19.
1056 Nikic, I., Estrada Girona, G., Kang, J.H., Paci, G., Mikhaleva, S., Koehler, C., Shymanska,
1057 N.V., Ventura Santos, C., Spitz, D., and Lemke, E.A. (2016). Debugging Eukaryotic Genetic
1058 Code Expansion for Site-Specific Click-PAINT Super-Resolution Microscopy. Angewandte
1059 Chemie *55*, 16172-16176.
1060 Nikic, I., and Lemke, E.A. (2015). Genetic code expansion enabled site-specific dual-color
1061 protein labeling: superresolution microscopy and beyond. Current opinion in chemical
1062 biology *28*, 164-173.
1063 Pear, W.S., Nolan, G.P., Scott, M.L., and Baltimore, D. (1993). Production of high-titer
1064 helper-free retroviruses by transient transfection. Proceedings of the National Academy of
1065 Sciences of the United States of America *90*, 8392-8396.
1066 Peng, K., Muranyi, W., Glass, B., Laketa, V., Yant, S.R., Tsai, L., Cihlar, T., Muller, B., and
1067 Krausslich, H.G. (2014). Quantitative microscopy of functional HIV post-entry complexes
1068 reveals association of replication with the viral capsid. eLife *3*.
1069 Pereira, C.F., Ellenberg, P.C., Jones, K.L., Fernandez, T.L., Smyth, R.P., Hawkes, D.J.,
1070 Hijnen, M., Vivet-Boudou, V., Marquet, R., Johnson, I.*, et al.* (2011). Labeling of multiple
1071 HIV-1 proteins with the biarsenical-tetracysteine system. PloS one *6*, e17016.
1072 Pizzato, M., Erlwein, O., Bonsall, D., Kaye, S., Muir, D., and McClure, M.O. (2009). A one-
1073 step SYBR Green I-based product-enhanced reverse transcriptase assay for the quantitation of
1074 retroviruses in cell culture supernatants. Journal of virological methods *156*, 1-7.
1075 Pornillos, O., Ganser-Pornillos, B.K., Kelly, B.N., Hua, Y., Whitby, F.G., Stout, C.D.,
1076 Sundquist, W.I., Hill, C.P., and Yeager, M. (2009). X-ray structures of the hexameric building
1077 block of the HIV capsid. Cell *137*, 1282-1292.

1078 Price, A.J., Fletcher, A.J., Schaller, T., Elliott, T., Lee, K., KewalRamani, V.N., Chin, J.W.,
1079 Towers, G.J., and James, L.C. (2012). CPSF6 defines a conserved capsid interface that
1080 modulates HIV-1 replication. PLoS pathogens *8*, e1002896.
1081 Price, A.J., Jacques, D.A., McEwan, W.A., Fletcher, A.J., Essig, S., Chin, J.W., Halambage,
1082 U.D., Aiken, C., and James, L.C. (2014). Host cofactors and pharmacologic ligands share an
1083 essential interface in HIV-1 capsid that is lost upon disassembly. PLoS pathogens *10*,
1084 e1004459.
1085 Rankovic, S., Ramalho, R., Aiken, C., and Rousso, I. (2018). PF74 Reinforces the HIV-1
1086 Capsid To Impair Reverse Transcription-Induced Uncoating. Journal of virology *92*.
1087 Rensen, E., Mueller, F., Scoca, V., Parmar, J.J., Souque, P., Zimmer, C., and Di Nunzio, F.
1088 (2021). Clustering and reverse transcription of HIV-1 genomes in nuclear niches of
1089 macrophages. The EMBO journal *40*, e105247.
1090 Rihn, S.J., Wilson, S.J., Loman, N.J., Alim, M., Bakker, S.E., Bhella, D., Gifford, R.J., Rixon,
1091 F.J., and Bieniasz, P.D. (2013). Extreme genetic fragility of the HIV-1 capsid. PLoS
1092 pathogens *9*, e1003461.
1093 Rust, M.J., Bates, M., and Zhuang, X. (2006). Sub-diffraction-limit imaging by stochastic
1094 optical reconstruction microscopy (STORM). Nature methods *3*, 793-795.
1095 Saito, A., and Yamashita, M. (2021). HIV-1 capsid variability: viral exploitation and evasion
1096 of capsid-binding molecules. Retrovirology *18*, 32.
1097 Sakin, V., Hanne, J., Dunder, J., Anders-Osswein, M., Laketa, V., Nikic, I., Krausslich, H.G.,
1098 Lemke, E.A., and Muller, B. (2017). A Versatile Tool for Live-Cell Imaging and Super-
1099 Resolution Nanoscopy Studies of HIV-1 Env Distribution and Mobility. Cell chemical
1100 biology *24*, 635-645 e635.
1101 Schaller, T., Ocwieja, K.E., Rasaiyaah, J., Price, A.J., Brady, T.L., Roth, S.L., Hue, S.,
1102 Fletcher, A.J., Lee, K., KewalRamani, V.N*., et al.* (2011). HIV-1 capsid-cyclophilin
1103 interactions determine nuclear import pathway, integration targeting and replication
1104 efficiency. PLoS pathogens *7*, e1002439.
1105 Schindelin, J., Arganda-Carreras, I., Frise, E., Kaynig, V., Longair, M., Pietzsch, T.,
1106 Preibisch, S., Rueden, C., Saalfeld, S., Schmid, B*., et al.* (2012). Fiji: an open-source platform
1107 for biological-image analysis. Nature methods *9*, 676-682.
1108 Schmied, W.H., Elsasser, S.J., Uttamapinant, C., and Chin, J.W. (2014). Efficient multisite
1109 unnatural amino acid incorporation in mammalian cells via optimized pyrrolysyl tRNA
1110 synthetase/tRNA expression and engineered eRF1. Journal of the American Chemical Society
1111 *136*, 15577-15583.
1112 Schorb, M., Gaechter, L., Avinoam, O., Sieckmann, F., Clarke, M., Bebeacua, C., Bykov,
1113 Y.S., Sonnen, A.F., Lihl, R., and Briggs, J.A.G. (2017). New hardware and workflows for
1114 semi-automated correlative cryo-fluorescence and cryo-electron microscopy/tomography.
1115 Journal of structural biology *197*, 83-93.
1116 Selyutina, A., Persaud, M., Lee, K., KewalRamani, V., and Diaz-Griffero, F. (2020). Nuclear
1117 Import of the HIV-1 Core Precedes Reverse Transcription and Uncoating. Cell reports *32*,
1118 108201.
1119 Shi, J., Zhou, J., Shah, V.B., Aiken, C., and Whitby, K. (2011). Small-molecule inhibition of
1120 human immunodeficiency virus type 1 infection by virus capsid destabilization. Journal of
1121 virology *85*, 542-549.
1122 Thenin-Houssier, S., and Valente, S.T. (2016). HIV-1 Capsid Inhibitors as Antiretroviral
1123 Agents. Current HIV research *14*, 270-282.
1124 Varadi, K., Michelfelder, S., Korff, T., Hecker, M., Trepel, M., Katus, H.A., Kleinschmidt,
1125 J.A., and Muller, O.J. (2012). Novel random peptide libraries displayed on AAV serotype 9
1126 for selection of endothelial cell-directed gene transfer vectors. Gene therapy *19*, 800-809.

von Schwedler, U.K., Stray, K.M., Garrus, J.E., and Sundquist, W.I. (2003). Functional surfaces of the human immunodeficiency virus type 1 capsid protein. Journal of virology *77*, 5439-5450.

Wang, L., Frei, M.S., Salim, A., and Johnsson, K. (2019). Small-Molecule Fluorescent Probes for Live-Cell Super-Resolution Microscopy. Journal of the American Chemical Society *141*, 2770-2781.

Wei, X., Decker, J.M., Liu, H., Zhang, Z., Arani, R.B., Kilby, J.M., Saag, M.S., Wu, X., Shaw, G.M., and Kappes, J.C. (2002). Emergence of resistant human immunodeficiency virus type 1 in patients receiving fusion inhibitor (T-20) monotherapy. Antimicrobial agents and chemotherapy *46*, 1896-1905.

Weigel, P.H., and Oka, J.A. (1981). Temperature dependence of endocytosis mediated by the asialoglycoprotein receptor in isolated rat hepatocytes. Evidence for two potentially rate-limiting steps. The Journal of biological chemistry *256*, 2615-2617.

Xu, H., Franks, T., Gibson, G., Huber, K., Rahm, N., Strambio De Castillia, C., Luban, J., Aiken, C., Watkins, S., Sluis-Cremer, N.*, et al.* (2013). Evidence for biphasic uncoating during HIV-1 infection from a novel imaging assay. Retrovirology *10*, 70.

Zhang, C., Zhou, X., Yao, T., Tian, Z., and Zhou, D. (2018). Precision Fluorescent Labeling of an Adeno-Associated Virus Vector to Monitor the Viral Infection Pathway. Biotechnology journal *13*, e1700374.

Zila, V., Margiotta, E., Turonova, B., Muller, T.G., Zimmerli, C.E., Mattei, S., Allegretti, M., Borner, K., Rada, J., Muller, B.*, et al.* (2021a). Cone-shaped HIV-1 capsids are transported through intact nuclear pores. Cell *184*, 1032-1046 e1018.

Zila, V., Muller, T.G., Laketa, V., Muller, B., and Krausslich, H.G. (2019). Analysis of CA Content and CPSF6 Dependence of Early HIV-1 Replication Complexes in SupT1-R5 Cells. mBio *10*.

Zila, V., Muller, T.G., Muller, B., and Krausslich, H.G. (2021b). HIV-1 capsid is the key orchestrator of early viral replication. PLoS pathogens *17*, e1010109.

Zurnic Bonisch, I., Dirix, L., Lemmens, V., Borrenberghs, D., De Wit, F., Vernaillen, F., Rocha, S., Christ, F., Hendrix, J., Hofkens, J.*, et al.* (2020). Capsid-Labelled HIV To Investigate the Role of Capsid during Nuclear Import and Integration. Journal of virology *94*.

1158 **Figures**

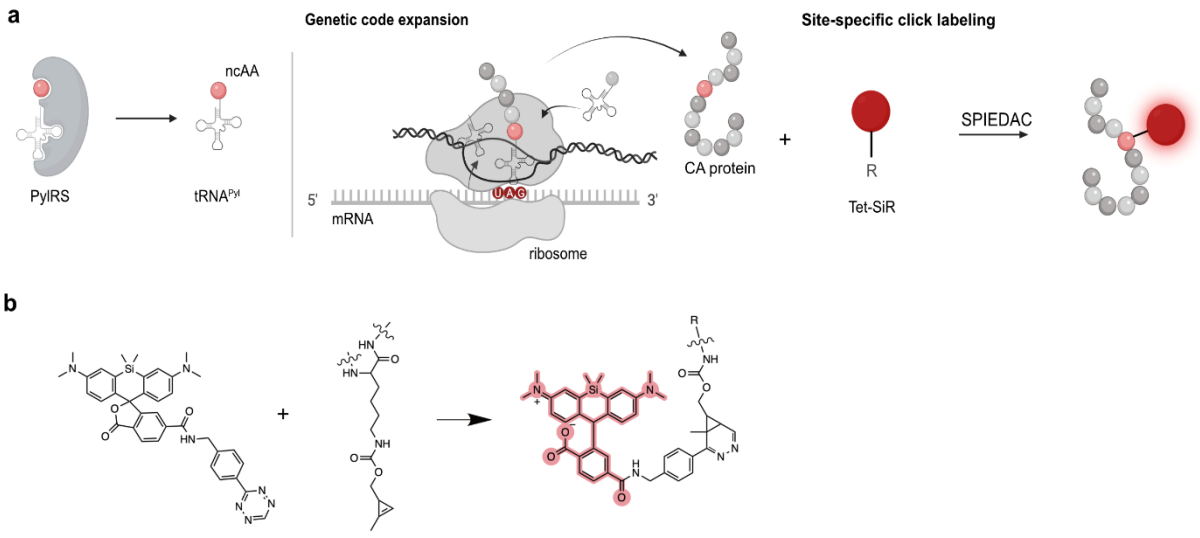

1159

1160 **Figure 1. GCE and click labeling of HIV-1 CA. (a)** Experimental scheme for GCE
1161 and click-labeling. The system used here requires the introduction of an amber stop
1162 codon (UAG) at a specific site into the CA coding sequence. A genetically engineered
1163 bio-orthogonal tRNA / aminoacyl-tRNA synthetase pair mediates incorporation of a
1164 non-canonical amino acid (ncAA) at the chosen position. In a second step, a highly
1165 reactive group of the ncAA is covalently linked to a fluorophore carrying a cognate
1166 reactive group (e.g., a tetrazine group reacting with a cyclopropene group at the ncAA
1167 via strain-promoted inverse electron-demand Diels-Alder cycloaddition (SPIEDAC)).
1168 Image created with BioRender.com. **(b)** The tetrazine-derivative of silicon rhodamine
1169 (Tet-SiR) reacts with the strained alkene of the ncAA cyclopropene-L-lysine (CpK) via
1170 SPIEDAC. The open SiR conformation results in fluorescence (highlighted in red).

1171

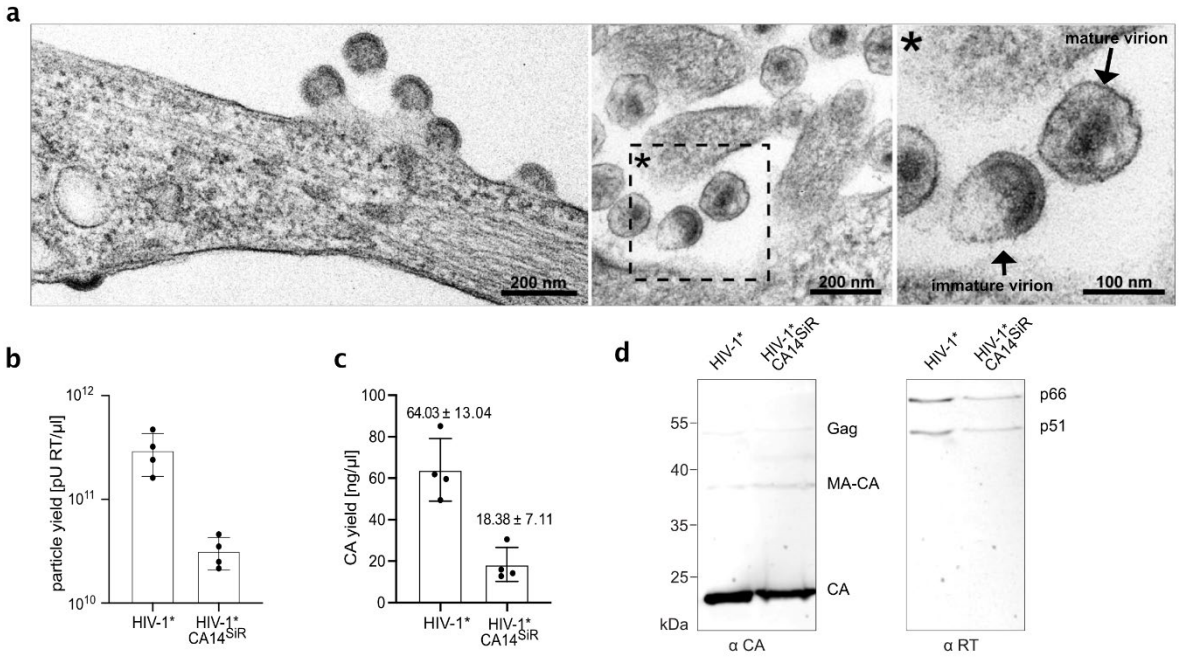

Figure 2. Production and characterization of click labeled HIV-1 (HIV-1*CA14^{SiR}). **(a)** Morphology of HIV-1*CA14^{ncAA} assembly sites and particles. HEK293T cells were co-transfected with pNLC4-3*CA14^{TAG} and pNESPylRS-eRF1dn-tRNA and grown in the presence of 500 µM CpK. At 44 h p.t., cells were fixed, embedded, and analyzed by thin-section EM as described in materials and methods. **(b,c)** Virus production. Click labeled particles were prepared from the supernatant of HEK293T cells co-transfected with either pNLC4-3* or pNLC4-3*CA14^{TAG} and pNESPylRS-eRF1dn-tRNA and grown in the presence of 500 µM CpK as described in materials and methods. Particle yield in the final preparations was determined via quantitation of RT activity (SG-PERT assay; (Pizzato et al., 2009)) (b) and by determination of CA amounts using quantitative immunoblot as described in materials and methods (c). The graphs show mean values and SD from four independent experiments. **(d)** Immunoblot analysis of virus preparations. 5 µl HIV-1* and HIV-1*CA14^{SiR} particle lysates were separated by SDS-PAGE, and proteins were transferred to nitrocellulose membranes by semi-dry blotting. Viral proteins were detected using the indicated polyclonal antisera. Bound antibodies were detected by quantitative immunofluorescence with a Li-COR CLx infrared scanner, using secondary antibodies and protocols according to the manufacturer's instructions. Positions corresponding to Gag/Gag-Pol and processing products are indicated to the right.

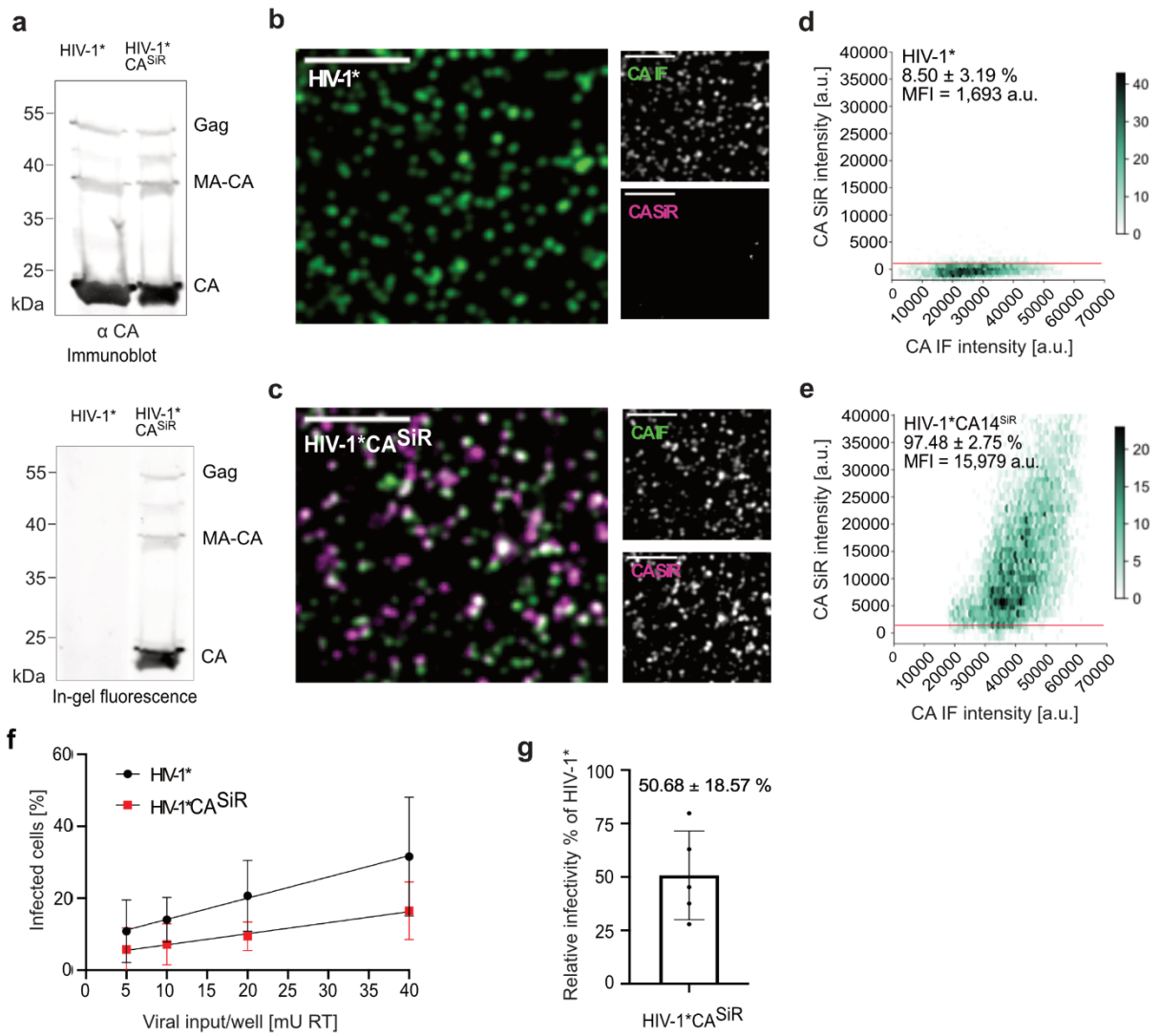

Figure 3. Characterization of CA click labeled particles. (a) Specific fluorescent labeling of CA14^{CpK}. Immunoblot analysis of virus preparations. 20 µl HIV-1* and HIV-1*CA14^{SiR} particle lysates were separated by SDS-PAGE. In-gel fluorescence (bottom panel) was detected by scanning the gel on a Li-COR Clx infrared scanner set at an emission wavelength of 700 nm. Subsequently immunoblot analysis (top panel) was performed using the previously scanned gel. Proteins were transferred from the gel to a nitrocellulose membrane by semi-dry blotting. Viral proteins were detected using polyclonal antiserum raised against recombinant CA. Bound antibodies were detected by quantitative immunofluorescence with a Li-COR CLx infrared scanner, using secondary antibody and protocol according to the manufacturer's instructions. Please note that at the high amounts of particles loaded for efficient in-gel fluorescence detection the immunoblot detection is not within the linear range of the method, so that contaminating precursor bands appear overrepresented. **(b-e)** Analysis of labeling efficiency. Particles harvested from the supernatant of virus producing HEK239T cells

1208 were subjected to click labeling. Particles were then immobilized on PEI coated
1209 chamber slides, fixed, and permeabilized. Particles were immunostained using
1210 antiserum raised against HIV-1 CA, and specimens were imaged by SDCM (b,c). Scale
1211 bars 5 µm. **(d,e)** Hexabin plots of particles detected in (b,c). Mean intensities of
1212 CA(SiR) are plotted against mean intensity CA(IF) for HIV-1* and HIV-1*CA14^{SiR}. The
1213 color intensity of the hexagons corresponds to the number of particles displaying the
1214 indicated intensity values. The graphs represent pooled data from 12 fields of view
1215 from three independent virus preparations. The red line indicates the threshold
1216 t=1,000. **(f)** Infectivity of click labeled particles. The indicated virus particles were
1217 prepared as in (b-e) and subjected to click labeling. Particle yield was assessed by RT
1218 activity assay (Pizzato et al., 2009), and samples were titrated on TZM-bl indicator cells
1219 seeded in 15-well ibidi µ-slide angiogenesis dishes. 50 µM T-20 was added at 6 h p.i.
1220 to prevent second-round infection in the case of HIV-1*. Cells were fixed,
1221 permeabilized, and immunostained using a polyclonal rabbit antiserum raised against
1222 recombinant HIV-1 MA at 48 h p.i. Samples were imaged by SDCM. The percentage
1223 of infected cells was determined using Fiji software. The graphs show mean values
1224 and SD from six independent infection experiments using five independent particle
1225 preparations (n=5,700-7,700 cells were counted per condition). Lines represent linear
1226 regression based on the mean values. **(g)** Relative infectivity of a virus preparation (%
1227 infected cells/mU RT) was determined as in (f), and the values obtained for HIV-
1228 1*CA14^{SiR} were normalized to the value obtained for HIV-1* virus in the same
1229 experiment. All cells counted in (f) were used for quantification. The graph represents
1230 the mean value and SD from six independent experiments.

1231

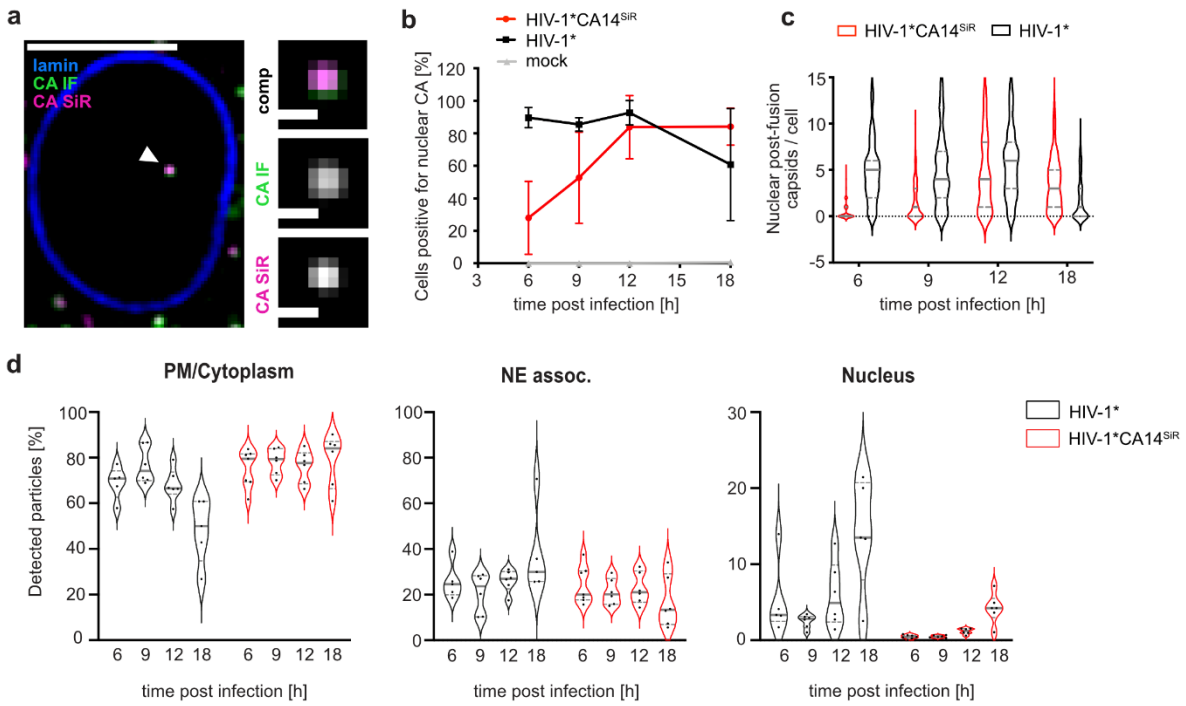

Figure 4. Detection of CA in the nucleus of infected HeLa-derived cells. TZM-bl cells were infected with HIV-1* or HIV-1* CA14^{SiR} particles (~MOI 0.8), treated with 15 µM PF74 for 1 h before fixation, fixed at 6, 9, 12 and 18 h p.i. and imaged by SDCM. **(a)** Single z slice of a representative cell infected with HIV-1* CA14^{SiR} at 18 h p.i. and one enlarged z slice are shown. Scale bars: 10 µm (cell) and 1 µm (enlargement). Mean filter and background subtraction was applied for clarity. The image shows a representative image from one of three independent experiments. See Figure S5 for additional data. **(b-d)** Infection time course of click labeled HIV-1* CA14^{SiR} compared to HIV-1*. Quantification of cells containing nuclear CA positive objects at the indicated times post infection for HIV-1* (black; CA(IF)), HIV-1* CA14^{SiR} (red; CA(IF)/CA(SiR)) and noninfected control (grey; CA(IF)). Mean values and SD from three independent experiments are shown (n>115 cells per timepoint). **(c)** Number of nuclear CA foci per cell determined for cells infected with HIV-1* (black) or HIV-1* CA14^{SiR} (red) at the indicated timepoints. n>120 cells were analyzed per sample. The median and interquartile lines are indicated in grey. **(d)** Localization of particles within the cell for HIV-1* (black) and HIV-1* CA14^{SiR} (red). The proportion of total particles per cell detected at the PM or in the cytoplasm (= PM/cytoplasm) at the nuclear envelope (=NE assoc.) or inside the nucleus was determined at the indicated time points. Data from two of three independent experiments are shown. Graphs show median of analyzed field of views in red (n>20 cells per condition) and interquartile lines.

1253

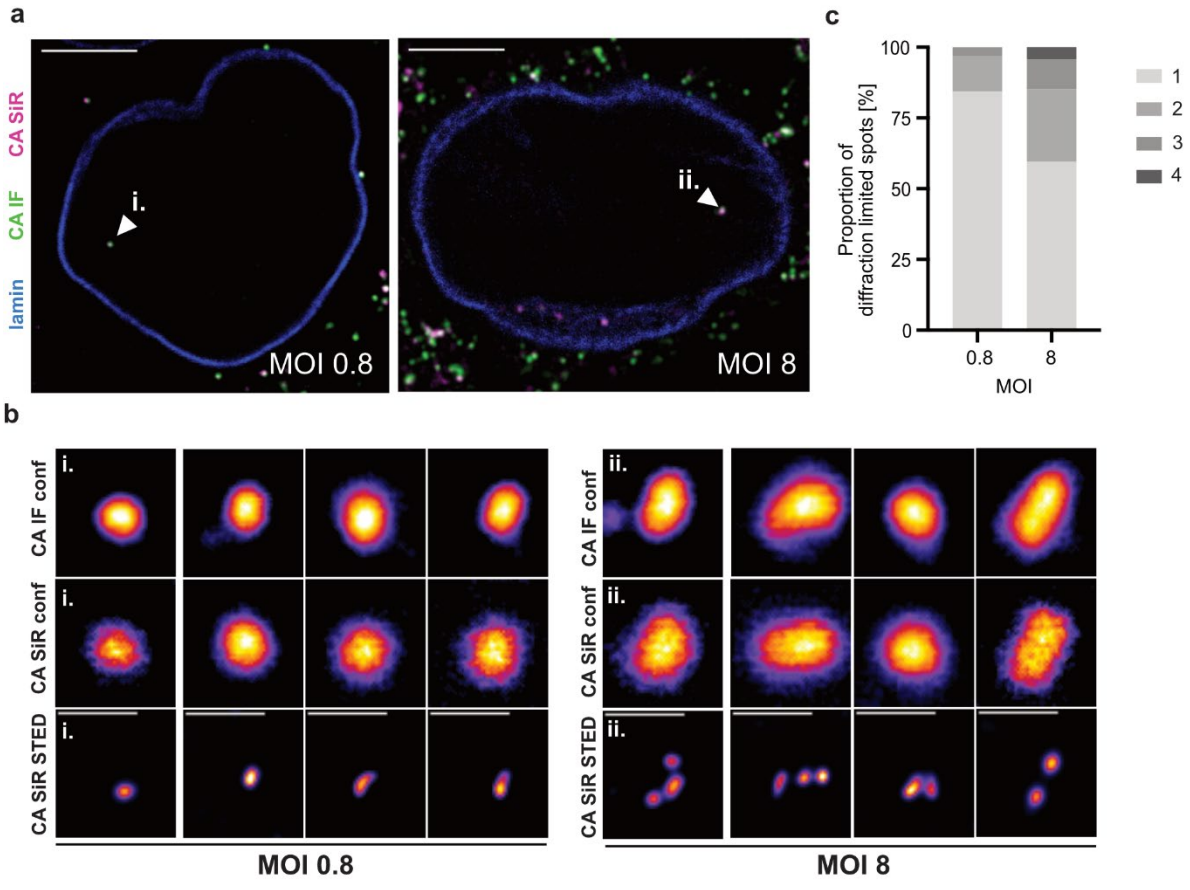

1254

1255 **Figure 5. Dose dependent clustering of nuclear capsids in HeLa-derived cells.**
1256 TZM-bl cells were infected with HIV-1* CA14^{SiR} at the indicated MOI, treated with 15 µM
1257 PF74 for 1 h before fixation at 18 h p.i., immunostained against CA (green) and lamin
1258 A/C (blue) and imaged using an Abberior STED microscope setup. Mean filter and
1259 background subtraction was applied to all images for clarity. **(a)** Micrographs of TZM-
1260 bl cells infected with MOI ~0.8 (left) or MOI ~8 (right). Arrowheads indicate nuclear
1261 CA(IF)/CA(SiR) positive objects shown enlarged in (b). Scale bars: 10 µm. **(b)**
1262 Representative images of nuclear CA containing objects from cells infected with a low
1263 MOI (MOI~0.8, left panel) or a high MOI (MOI~8, right panel). CA(IF) and CA(SiR)
1264 were imaged in confocal mode (top and middle row, respectively). CA(SiR) images
1265 were also recorded in STED mode (bottom row). The figure shows four representative
1266 foci each from one of two individual experiments. Mean filter and background
1267 subtraction were applied. Scale bars: 500 nm. **(c)** Diffraction-limited nuclear foci were
1268 analyzed by STED nanoscopy in cells infected with MOI~0.8 (n = 32 foci) or MOI~8 (n
1269 =47 foci) and classified by the number of individual capsids per focus.

1270

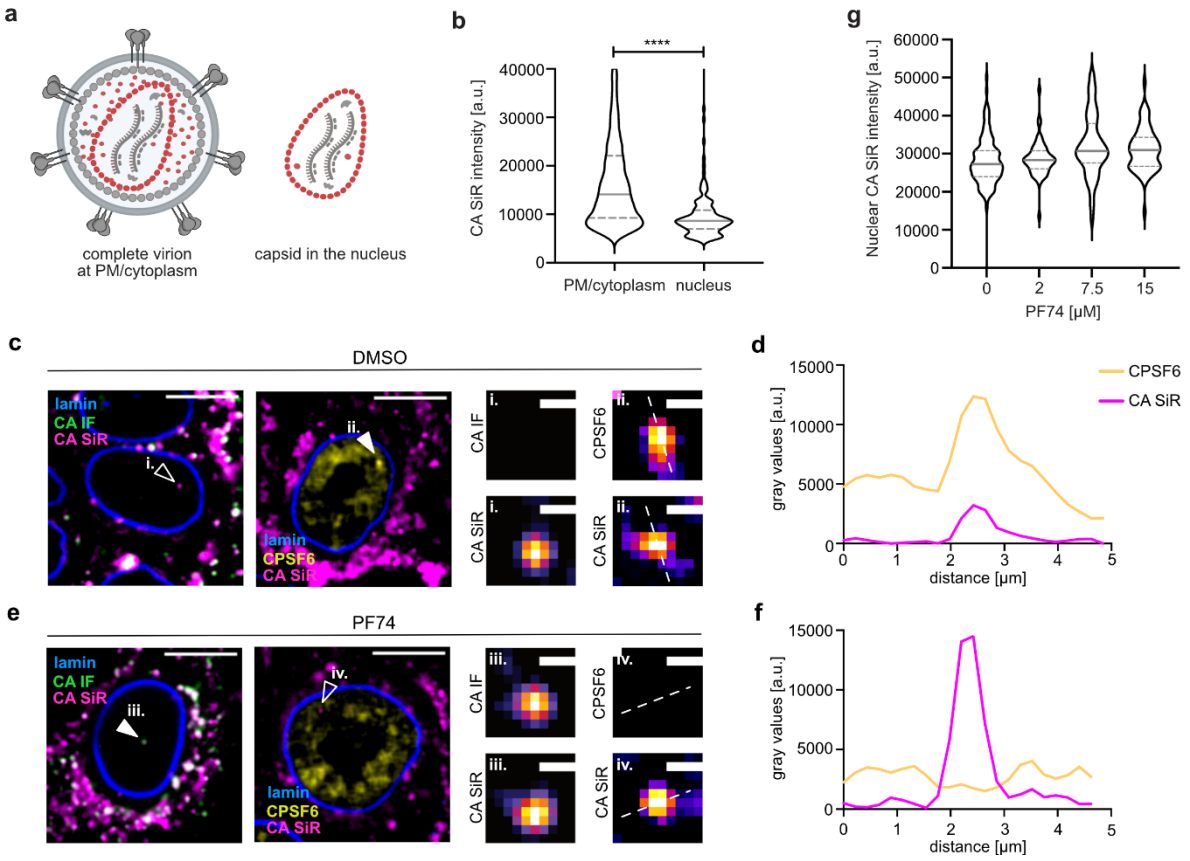

Figure 6. Largely intact capsids are detected in the nucleus of HeLa-derived cells. TZM-bl cells were infected with HIV-1* or HIV-1* CA14^{SiR} (MOI~0.8), treated with 15 µM PF74 for 1 h before fixation at 18 h p.i. and imaged by SDCM. **(a)** Scheme of the relative CA content in complete virions (~2,400 CA) on glass/plasma membrane or in endosomes in the cytosol. Post-fusion capsids contain only the CA molecules incorporated into the mature capsid lattice (~1,500 CA). Image created with BioRender. **(b)** Quantification of CA(SiR) intensities associated with CA(IF) positive objects at the indicated localizations. Data from three independent experiments are shown. Cells from 7 fields of view were analyzed ($n_{particles}$= 6,441 PM/cytoplasm, 135 nucleus). Lines indicate median values (PM/cytoplasm: 17,649.22 ± 11,663.47; nucleus: 9,835.08 ± 5,708.14) and interquartile range. Significance was determined by two-tailed Student`s t-test (*** < 0.001). **(c-g)** TZM-bl cells were infected with HIV-1*CA14^{SiR}, treated with DMSO **(c,d)** or 15 µM PF74 **(e,f)** for 1h before fixation at 18 h p.i.. Cells were immunostained against lamin A/C and HIV-1 CA or CPSF6 and subsequently imaged by SDCM. Scale bars: 10 µm (cells) and 1 µm (enlargements). **(d)** Quantification of intensity profile measured across the dashed line in **(c,ii.)** for CA(SiR) and CPSF6. **(f)** Quantification of intensity profile measured across the dashed line in **(e,iv.)** for CA (SiR) and CPSF6. **(g)** Quantification of CA(SiR) intensities of nuclear objects. TZM-bl cells

1290 were treated with DMSO (n=115) or 2 µM (n=58), 7.5 µM (n=110), 15 µM (n=69) PF74
1291 for 1 h prior fixation at 17 h p.i.. Graphs show median values (DMSO: 2,7255; 2 µM:
1292 2,8334.51; 7.5 µM: 3,0749.45; 15 µM: 3,0957) and interquartile range.

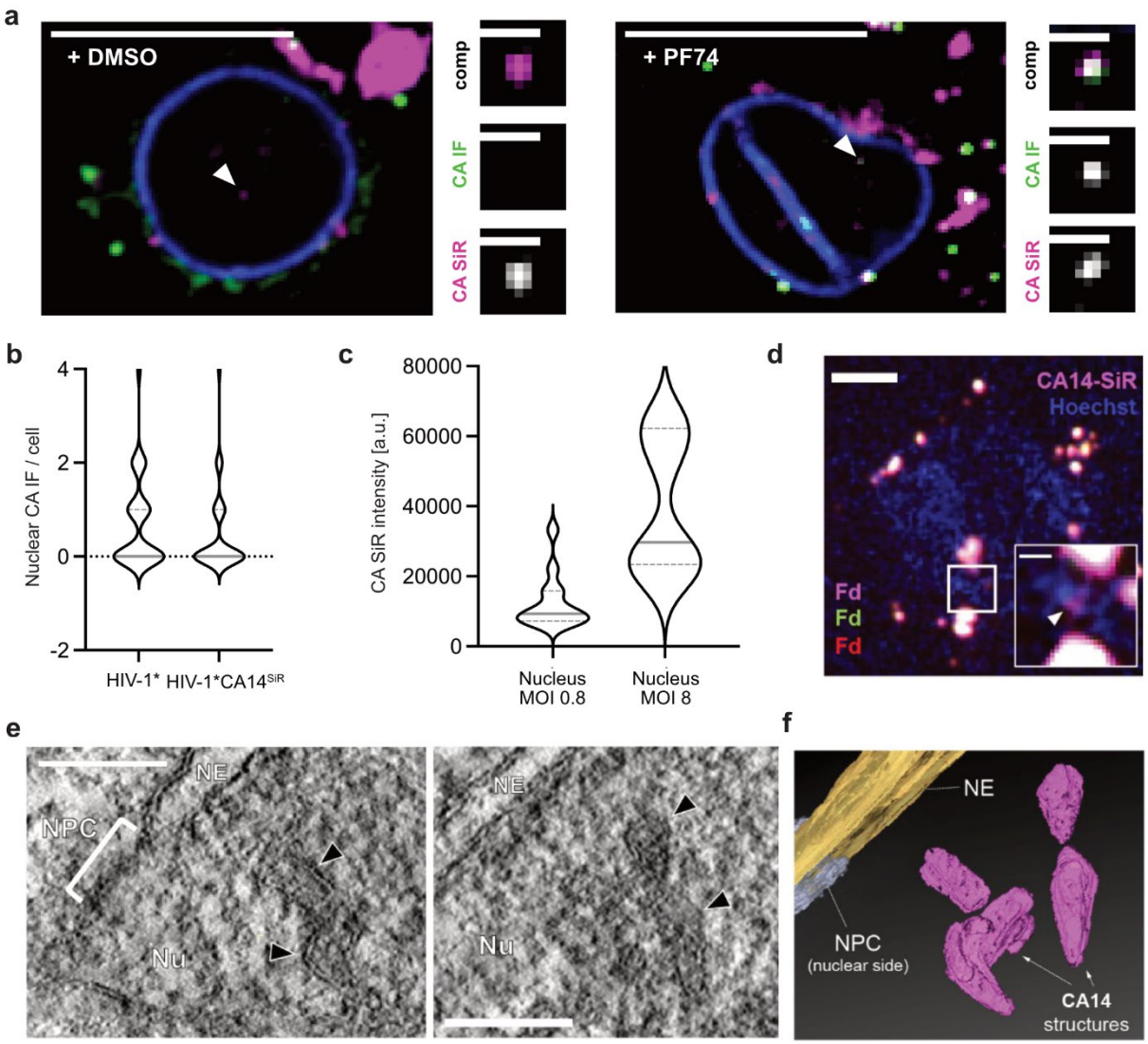

Figure 7. Largely complete click labeled capsid structures detected in the nucleus of primary CD4⁺ T cells and T cell line. (a) Activated CD4⁺ T cells were infected with HIV-1*CA14^{SiR} (MOI~0.8), treated with DMSO/PF74 treatment for 1 h before fixation at 24 h p.i., and extracted with methanol. Samples were immunostained against CA (green) and lamin A/C (blue). Images show a single z slice through the cell. Enlargements show the particle marked by the arrowhead. Scale bars: 10 µm (overview) and 1 µm (enlargement). **(b)** Data analyzed from the experiment outlined in (a). The graph shows the number of CA positive foci per nucleus in cells infected with HIV-1* (n=35 cells, mean=0.85) or HIV-1*CA14^{SiR} (n= 73 cells, mean=0.51). Pooled data from 6 different blood donors are shown. Grey lines show median and interquartile lines. **(c)** CA(SiR) intensities of nuclear objects in infected and activated CD4⁺ T cells at an MOI~0.8 (n=13; mean=12,485 ± 7,445 a.u.) and an MOI ~8 (n=7; mean=39,502 ± 18,025 a.u.). MOI was determined in TZM-bl cells. Grey lines show median and interquartile lines. **(d-f)** Nuclear cone-shaped capsids detected by CLEM-ET. SupT1

1308 cells were treated with 1 µM aphidicolin (APC) for 16 h to prevent cell division, before
1309 infection with HIV-1*CA14^{SiR} virions (2.3 µU RT/cell, corresponds to an MOI~0.4
1310 determined in TZM-bl cells). At 24 h p.i., cells were cryo-immobilized by high-pressure
1311 freezing, freeze substituted, and further processed for CLEM and ET as described in
1312 materials and methods. **(d)** SDCM image of a 250-nm thick resin section of the cell
1313 infected with HIV-1*CA14^{SiR} virions (magenta), post-stained with Hoechst (blue) and
1314 decorated with multi-fluorescent fiducials (Fd) for correlation. The arrowhead in the
1315 enlargement of the boxed region indicates a CA(SiR) signal within the Hoechst-stained
1316 nuclear region. Scale bars: 1 µm (overview) and 200 nm (enlargement). **(e)**
1317 Computational slices through tomographic reconstructions at the correlated region
1318 boxed in (d) with views highlighting the presence of clustered capsid-reminiscent
1319 structures (black arrowheads) in the nuclear region. Nu, nucleus; NPC, nuclear pore
1320 complex; NE, nuclear envelope. Scale bar: 100 nm. **(f)** Segmented and isosurface
1321 rendered structure of the cones detected in (e). Magenta: capsid, yellow: NE, cyan:
1322 NPC (cryo-EM map of NPC: EMD-11967 (Zila et al., 2021a)). See also supplementary
1323 movie 1.